Journal of Fluids and Structures 98 (2020) 103135

Contents lists available at ScienceDirect

Journal of Fluids and Structures

journal homepage: www.elsevier.com/locate/jfs

Identification of upper branch for vortex-induced vibration of a circular cylinder at $Re = 300$

Dániel Dorogi *, László Baranyi

Department of Fluid and Heat Engineering, University of Miskolc, 3515 Miskolc-Egyetemváros, Hungary

ARTICLE INFO

Article history:
Received 11 February 2020
Received in revised form 4 June 2020
Accepted 24 August 2020
Available online xxxx

Keywords:
CFD
Low Reynolds number
Phase differences
second harmonic component
Upper branch
Vortex-induced vibration

ABSTRACT

In this study flow around a circular cylinder undergoing transverse-only vortex-induced vibrations is investigated using a two-dimensional in-house CFD code. The Navier–Stokes equations, the continuity and pressure Poisson equations written for an incompressible constant property Newtonian fluid coupled with the structural equation are solved using the finite difference method. Systematic computations are carried out for different damping ratio values between $\zeta = 0\%$ and 5%. Reduced velocity is varied in $U^* = 2.5 - 7.5$, while Reynolds number and mass ratio are fixed at $Re = 300$ and $m^* = 10$, respectively. Up until now, researchers have reported an upper branch only at high Reynolds numbers and low $m^*\zeta$ values. However, in this study we have observed a three-branch behavior (initial, upper and lower branches) at $Re = 300$ for $\zeta \leq 1\%$. The upper branch is bounded by two gradual phase changes: at the boundary adjacent to the initial branch, the time-averaged phase difference of vortex force, and at the boundary to the lower branch, the time-averaged phase difference of transverse fluid force relative to the cylinder displacement changes between 0° and 180°. Unbounded variations and phase slips are observed in the time-dependent phase differences, which explains the gradual changes in their time-mean values. In some ranges of the upper branch the second harmonic frequency component plays an important role in the spectra of transverse fluid force, which is closely related to the observed asymmetrical vortex structure. Increasing the structural damping above $\zeta = 1\%$, only initial and lower branches are found. The comparison of peak oscillation amplitude against an empirical relationship provided in the literature shows very good agreement for $\zeta \geq 1\%$. A Griffin plot is also used for the comparison of peak response data where the currently obtained results and those in the literature collapse onto almost a single curve.

1. Introduction

Fluid flow around bluff bodies has been thoroughly investigated in the past few decades due to its large number of engineering applications. It plays an important role for instance in offshore structures, high slender buildings or heat exchangers. Vortices shedding from bluff bodies can induce the vibration of the structure, which is referred to as *vortex-induced vibrations* (VIV). Various effects of VIV were shown for example by Bearman (1984, 2011), Blevins (1990), Sarpkaya (2004), and Williamson and Govardhan (2004).

* Corresponding author.
E-mail addresses: aramdd@uni-miskolc.hu (D. Dorogi), arambl@uni-miskolc.hu (L. Baranyi).

https://doi.org/10.1016/j.jfluidstructs.2020.103135

Nomenclature

Latin symbols

b	Structural damping [kg s^{-1}]
C_v	Vortex force coefficient, $2F_v/(\rho U_\infty^2 d)$ [–]
C_A	Added mass coefficient [–]
C_y	Transverse fluid force coefficient, $2F_y/(\rho U_\infty^2 d)$ [–]
D	Dilation, non-dimensionalized by U_∞/d
d	Cylinder diameter, length scale [m]
f^*	Vibration frequency, non-dimensionalized by U_∞/d
$f^*_{C_v}$	Frequency of vortex force, non-dimensionalized by U_∞/d
$f^*_{C_y}$	Frequency of transverse fluid force, non-dimensionalized by U_∞/d
f_N	Natural frequency of the cylinder in vacuum, $1/(2\pi)\sqrt{k/m}$ [s^{-1}]
F_p	Potential added mass force per unit length of the cylinder [N m^{-1}]
F_v	Vortex force per unit length of the cylinder [N m^{-1}]
F_y	Transverse fluid force per unit length of the cylinder [N m^{-1}]
f_{v0}	Vortex shedding frequency for a stationary cylinder [s^{-1}]
k	Spring constant [kg s^{-2}]
m	Cylinder mass per unit length [kg m^{-1}]
m^*	Mass ratio, $m^* = 4m/(\rho d^2 \pi)$ [–]
m_A	Added mass of fluid per unit length of the cylinder, $C_A \rho d^2 \pi/4$ [kg m^{-1}]
p	Pressure, non-dimensionalized by ρU_∞^2 [–]
R	Radius, non-dimensionalized by d [–]
Re	Reynolds number, $\rho U_\infty d/\mu$ [–]
St	Dimensionless vortex-shedding frequency for a stationary cylinder, Strouhal number, $f_{v0} d/U_\infty$ [–]
t	Time, non-dimensionalized by d/U_∞ [–]
u, v	Velocity components in x and y directions, non-dimensionalized by U_∞ [–]
U^*	Reduced velocity based on the cylinder's natural frequency in vacuum, $U_\infty/(f_N d)$ [–]
U_∞	Free steam velocity, velocity scale [m s^{-1}]
x, y	Cartesian coordinates, non-dimensionalized by d [–]
y_0	Cylinder displacement, non-dimensionalized by d [–]

Greek symbols

η_{max}	Number of grid points in radial direction [–]
Φ	Phase difference between C_y and y_0, transverse phase [–]
Φ_v	Phase difference between C_v and y_0, vortex phase [–]
μ	Dynamic viscosity of the fluid [Pa s]
ρ	Fluid density [kg m^{-3}]
ξ_{max}	Number of grid points in peripheral direction [–]
ζ	Structural damping ratio, $b/(2\sqrt{km})$ [–]

Subscripts and superscripts

x	Streamwise
y	Transverse
0	Cylinder response
1, 2	On the cylinder surface, at the outer boundary of the computational domain

In this study vortex-induced vibration of a circular cylinder is analyzed using a numerical approach. Although in reality the cylinder moves in two degrees of freedom (both streamwise with and transverse to the main stream), transverse-only vibration is often used to model VIV. Feng (1968), Brika and Laneville (1993), and Khalak and Williamson (1999) showed that the cylinder response (amplitude and frequency values) depends highly on the mass-damping parameter $m^*\zeta$, where m^* is the mass ratio (cylinder mass divided by the mass of the displaced fluid), and ζ is the structural damping ratio. Feng (1968) and Brika and Laneville (1993) investigated high-$m^*\zeta$ cases. Plotting the amplitude of cylinder oscillation against reduced velocity they found two response branches — initial and lower branches, where the initial branch was

associated with the peak oscillation amplitude. In addition, Brika and Laneville (1993) showed that the transition between initial and lower branches is hysteretic, due to the abrupt change in the vortex structure. Using the notations introduced by Williamson and Roshko (1988), Brika and Laneville (1993) observed 2*S* mode (two single vortices are shed from the cylinder in each motion cycle) in the initial branch, while 2*P* mode (two vortex pairs are shed) was present in the lower branch.

Khalak and Williamson (1999) identified three response branches (initial, upper, and lower branches) for very low mass-damping values, where peak vibration amplitude is associated with the upper branch. They found hysteresis in the initial↔upper branch transition range, whereas vortex structure switches between 2*S* and 2*P* modes. The transition between upper and lower branches is found to be intermittent, since the wake mode does not show changes (2*P* mode is observed both in the upper and lower branches). Govardhan and Williamson (2000) investigated also low mass-damping cases using experimental techniques. Following Lighthill (1986), Govardhan and Williamson (2000) decomposed the transverse fluid force into vortex force and potential added mass force components. The phase differences for transverse fluid force and vortex force relative to the cylinder displacement Φ and Φ_v were calculated using the Hilbert transform of the corresponding signals. They showed that Φ_v jumps between approximately 0° and 180° in the initial↔upper branch transition range, where the vortex structure switches from 2*S* to 2*P* mode. In this range the cylinder displacement remained in-phase with the transverse fluid force. However, in the transition domain between upper and lower branches (where no significant changes were identified in the wake mode) Φ was found to jump from 0° to 180°, and the vortex force remained out-of-phase with the cylinder displacement.

Klamo et al. (2006) investigated the effects of structural damping ratio and Reynolds number on the cylinder response. They showed that by increasing ζ the high-amplitude three-branch response switches to two-branch response, where the oscillation amplitude is significantly lower. Soti et al. (2018) carried out a systematic experimental study for different ζ values. In addition to the cylinder response, they analyzed the power transfer between the oscillating cylinder and the surrounding fluid. They identified three-branch response for a wide damping ratio range; they showed the occurrence of upper branch even at low oscillation amplitudes (down to $\hat{y}_0 = 0.2$, where $\hat{y}_0$ is the oscillation amplitude non-dimensionalized by the cylinder diameter). Bernitsas et al. (2008) and Lee and Bernitsas (2011) investigated the possibilities of energy harvesting from vortex-induced vibrations. Bernitsas et al. (2008) derived an analytical formula for the calculation of power transfer based on harmonic approximations. They found that power transfer is zero when Φ (or Φ_v) equals to 0° and 180°, i.e. for undamped vibrations. Their formula reveals also that increasing structural damping ratio, power transfer can be increased, which agrees well with the experimental results of Soti et al. (2018). Konstantinidis et al. (2019) analyzed energy transfer (analogous with the power transfer) from another perspective using laboratory measurements at very low mass-damping values. They decomposed the total hydrodynamic force acting on the cylinder into components parallel with and normal to the time-dependent vector of the cylinder's relative velocity, i.e. the drag and lift forces, respectively. They showed that drag does only negative work on the vibrating cylinder, while the work done by the lift is positive in most of the investigated cases.

Klamo et al. (2006) and Govardhan and Williamson (2006) showed that cylinder response is significantly influenced by Reynolds number $Re = \rho U_\infty d/\mu$, where ρ is the fluid density, U_∞ is the free stream velocity, d is the cylinder diameter, and μ is the dynamic viscosity of the fluid. Most of the experiments are carried out in the Reynolds number range of $Re = O(10^3 - 10^4)$. However, due to the high computational time demand numerical simulations are usually carried out in the low-Reynolds-number range [$Re = O(10^2)$]. Another issue is the three-dimensionality of the flow structure. Barkley and Henderson (1996), using linear stability analysis, found that the flow around a stationary cylinder is fully two-dimensional up to $Re \cong 189$. They reported three-dimensional (3D) instabilities at $Re \cong 189$ (Mode A) and at $Re \cong 259$ (Mode B). Koide et al. (2002) carried out laboratory measurements for a mechanically oscillated cylinder at the Reynolds number of $Re \cong 3500$. They demonstrated that the cross-correlation coefficient of the velocities measured at different locations along the cylinder's span significantly increases when the cylinder is oscillated at relatively large amplitudes. This effect indicates that the synchronization between cylinder vibration and vortex shedding (i.e. lock-in) increases the two-dimensionality of the flow. Bearman and Obasaju (1982) showed a similar phenomenon using fluctuating pressure measurements for a square cylinder: by oscillating the body at relatively high amplitudes, the spanwise coherency of the flow structure increases. Poncet (2002) carried out 3D computations at $Re = 500$ for a stationary cylinder, where Mode B instability developed. He showed that soon after beginning to apply high-amplitude rotary oscillations the three-dimensional instability vanished and the flow became fully two dimensional. Since there are several independent parameters for the case of a vibrating cylinder (e.g. Reynolds number, oscillation amplitude, and frequency values), the upper limit of the two-dimensionality has not yet been determined. There are several important studies in the literature performing 2D computations at higher Reynolds numbers ($Re > 189$). For example Blackburn and Henderson (1999) investigated the flow around a transversely oscillated cylinder at the Reynolds number of 500, while Singh and Mittal (2005) analyzed two-degree-of-freedom vortex-induced vibrations of a circular cylinder at *Re* ranging between 50 and 500.

Computational results available in the literature show that oscillation amplitudes for low Reynolds numbers are significantly lower ($\hat{y}_0 \cong 0.55$, see Navrose and Mittal, 2017) compared to high-*Re* experiments ($\hat{y}_0 \cong 0.8$, see Govardhan and Williamson, 2000). Anagnostopoulos and Bearman (1992) obtained similar characteristics using measurement techniques in the range of $Re = 90 - 150$. Using CFD simulations Leontini et al. (2006b) found two-branch cylinder response at the parameter combination of $Re = 200$, $m^* = 10$, and $\zeta = 1\%$. The vortex structures are markedly different from

those observed at high Reynolds numbers: $2S$ and $C(2S)$ wake modes were found in the initial and lower branches, respectively. Here C refers to the coalescence of the positive and negative vortices in the cylinder wake. Navrose and Mittal (2017) carried out numerical simulations at $Re = 100$ and $\zeta = 0\%$ using different mass ratio values in the range of $m^* = 30 - 150$. They found a narrow reduced velocity $U^* = U_\infty/(f_N d)$ range in the middle of the lower branch where the oscillation amplitude was low and the vibration frequency did not synchronize with the cylinder's natural frequency. They also showed that the width of this low-amplitude domain extends with m^*.

As was pointed out earlier, the vortex structures at low and high-Reynolds-number flows are quite different. Williamson and Roshko (1988) carried out forced vibration experiments in the range of $Re = 300 - 1000$, and created a wake mode map (the well-known Williamson-Roshko map). It can be seen from their results that the $2P$ vortex structure plays an important role in the fundamental lock-in domain, which was confirmed by the free vibration results of Brika and Laneville (1993), Khalak and Williamson (1997, 1999), and Govardhan and Williamson (2000). In addition, Williamson and Roshko (1988) identified the $P + S$ asymmetrical mode (a vortex pair and a single vortex are shed) at high vibration amplitudes ($\hat{y}_0 = 1 - 2$), which is not so typical in VIV cases. They found that decreasing the Reynolds number below $Re = 300$ the $2P$ mode in the fundamental synchronization range may be replaced by the $P + S$ vortex structure. The forced vibration CFD results of Meneghini and Bearman (1995) and Blackburn and Henderson (1999) confirmed this finding: they did not observe the $2P$ mode of vortex shedding but they found the $P + S$ vortex structure. Leontini et al. (2006a) carried out systematic forced vibration computations at $Re \leq 300$. Similar to the experiments of Williamson and Roshko (1988), Leontini et al. (2006a) investigated the effects of forcing frequency and amplitude and created wake mode maps at $Re = 100$ and 300. At $Re = 100$ the $P + S$ mode occurred only over $\hat{y}_0 = 0.9$. However, at $Re = 300$ they did identify the $P + S$ vortex structure around $\hat{y}_0 = 0.55$ (and near the fundamental lock-in domain) that can be reached in low-Re VIV.

The numerical studies investigating vortex-induced vibrations at low Reynolds numbers have not reported an upper branch even for undamped systems (see e.g. Leontini et al., 2006b and Navrose and Mittal, 2017). However, Evangelinos and Karniadakis (1999) reported that the $P + S$ vortex pattern may also be associated with the upper branch, which is rarely identified in VIV cases. Singh and Mittal (2005) investigated two-degree-of-freedom vortex-induced vibrations numerically, and found the $P + S$ vortex structures above $Re = 300$. Dorogi and Baranyi (2019) also observed the asymmetrical $P + S$ wake mode close to $Re = 300$, which caused an asymmetrical orbital ("raindrop-shaped") cylinder motion.

The main objective of this study is to explore whether an upper branch, i.e. three-branch cylinder response, can exist at the Reynolds number of $Re = 300$. To accomplish this aim, two-dimensional numerical simulations are carried out at this Reynolds number using mass ratio value of $m^* = 10$. Damping ratio values in the range of $\zeta = 0\%$ and 5% are considered, and reduced velocity is varied between $U^* = 2.5$ and 7.5. Oscillation amplitude and frequency, time-dependent and time-averaged phase angles, frequency spectra, and vortex structures are analyzed.

2. Governing equations and solution methodology

In this study vortex-induced vibration (VIV) of a circular cylinder placed into a uniform stream is investigated by means of CFD (*Computational Fluid Dynamics*) computations at low Reynolds numbers $Re = \rho U_\infty d/\mu$. Here ρ is the fluid density, U_∞ is the free stream velocity, d is the cylinder diameter and, μ is the dynamic viscosity of the fluid. The cylinder is elastically supported only in transverse direction. Its displacement, velocity, and acceleration values are obtained by solving Newton's second law of motion. This equation in non-dimensional form can be written as follows:

$$\ddot{y}_0 + \frac{4\pi\zeta}{U^*}\dot{y}_0 + \left(\frac{2\pi}{U^*}\right)^2 y_0 = \frac{2C_y}{\pi m^*}, \tag{1}$$

where y_0, $\dot{y}_0$, and $\ddot{y}_0$ are the dimensionless cylinder displacement, velocity, and acceleration, respectively, $U^* = U_\infty/(f_N d)$ is the reduced velocity based on the cylinder's natural frequency in vacuum f_N, ζ is the damping ratio (structural over critical damping), and m^* is the ratio of the cylinder's mass to that of the displaced fluid, i.e. the mass ratio. On the right-hand side of Eq. (1) $C_y = 2F_y/(\rho U_\infty^2 d)$ is the transverse fluid force coefficient where F_y is the transverse fluid force per unit length of the cylinder.

The fluid is assumed to be two-dimensional incompressible constant property and Newtonian. Its motion is governed by the two components of the Navier–Stokes equations and the continuity equation. The equations of motion are written in a non-inertial frame of reference attached to the oscillating cylinder. These equations in non-dimensional forms are written as follows:

$$\frac{\partial u}{\partial t} + u\frac{\partial u}{\partial x} + v\frac{\partial u}{\partial y} = -\frac{\partial p}{\partial x} + \frac{1}{Re}\left(\frac{\partial^2 u}{\partial x^2} + \frac{\partial^2 u}{\partial y^2}\right), \tag{2}$$

$$\frac{\partial v}{\partial t} + u\frac{\partial v}{\partial x} + v\frac{\partial v}{\partial y} = -\frac{\partial p}{\partial y} + \frac{1}{Re}\left(\frac{\partial^2 v}{\partial x^2} + \frac{\partial^2 v}{\partial y^2}\right) - \ddot{y}_0, \tag{3}$$

$$D = \frac{\partial u}{\partial x} + \frac{\partial v}{\partial y} = 0. \tag{4}$$

Here x and y are the non-dimensional Cartesian coordinates in streamwise and transverse directions, respectively, u and v are the dimensionless velocity components in x and y directions, p is the dimensionless pressure, t is the non-dimensional time, and D is the dilation. Instead of solving Eq. (4) explicitly, a Poisson equation is derived and used for computing fluid pressure (Harlow and Welch, 1965 and Baranyi, 2008), which can be written in non-dimensional form as follows:

$$\nabla^2 p = \frac{\partial^2 p}{\partial x^2} + \frac{\partial^2 p}{\partial y^2} = 2\left(\frac{\partial u}{\partial x}\frac{\partial v}{\partial y} - \frac{\partial u}{\partial y}\frac{\partial v}{\partial x}\right) - \frac{\partial D}{\partial t}. \tag{5}$$

Although dilation is zero for an incompressible fluid, $\partial D/\partial t$ is kept in Eq. (5) to reduce numerical inaccuracies.

The physical domain of the computations is confined by two concentric circles. The dimensionless radius of the cylinder is denoted by R_1 while that of the far field by R_2. Dirichlet-type boundary conditions are applied for the two velocity components, and Neumann type of boundary condition is used for fluid pressure both on the cylinder surface $R = R_1$ and in the far field $R = R_2$ (see Baranyi, 2008). In order to obtain accurate results, the physical domain is transformed into a computational domain. It is advantageous that using appropriate mapping functions, on the physical domain the grid is fine in the vicinity of the cylinder and relatively coarse in the far field, while the mesh is equidistant in the computational domain. Following Baranyi (2008), linear mapping functions are used in this study.

An in-house CFD code based on finite difference method is used to solve the transformed governing equations with the transformed boundary conditions. Space derivatives are approximated using fourth-order accurate difference schemes except for the convective terms for which a third-order modified upwind difference scheme (developed by Kawamura et al., 1986) is employed. The linear algebraic equation system obtained from the discretization of pressure Poisson equation is solved using the successive over-relaxation (SOR) method, and continuity equation is satisfied in each time step. Fourth-order Runge–Kutta scheme is applied to determine the displacement, velocity, and acceleration of the cylinder, while the two components of the Navier–Stokes equations are integrated explicitly using the first-order Euler method. Additional details of the computational approach are given in Baranyi (2008).

3. Verification and validation

In this section, first, independence studies are carried out to determine the optimal combination of computational parameters. Afterwards, the results obtained using the in-house code are validated against those presented in Bourguet and Lo Jacono (2014) and Blackburn and Henderson (1996).

3.1. Independence studies

The currently applied in-house CFD approach is used with the following parameters: radius ratio R_2/R_1, grid resolution $\xi_{max} \times \eta_{max}$ (number of grid points in peripheral and radial directions, see details in Baranyi (2008)), and dimensionless time step Δt. In order to find the optimal combination of these computational parameters, which is the best compromise between accuracy and computational time, independence studies are required. During these investigations, Reynolds number, mass ratio, structural damping ratio, and reduced velocity are fixed at $Re = 300$, $m^* = 10$, $\zeta = 0\%$, and $U^* = 4.65$, respectively, and the cylinder is allowed to oscillate only in transverse direction. The root-mean-square (rms) values of cylinder displacement $y_{0'}$, dimensionless vibration frequency f^*, the rms values of transverse fluid force coefficient $C_{y'}$, and the time-mean and rms values of streamwise fluid force coefficient $\overline{C}_x$ and $C_{x'}$ are investigated.

First, the effect of radius ratio R_2/R_1 is analyzed. The number of grid points around the cylinder surface is fixed at $\xi_{max} = 360$, and the dimensionless time step is chosen to be $\Delta t = 10^{-4}U^* \cong 0.0004$. Radius ratio values of $R_2/R_1 = 200, 240$, and 280 are considered. In order to create an equidistant grid on the computational domain, the number of grid points in radial direction is varied with R_2/R_1; $\eta_{max} = 304, 314$, and 323 are applied. The results are shown in Table 1. It can be seen that $C_{y'}$ shows the highest relative difference; for $R_2/R_1 = 200$ and 240 its value is 1.47%. The time-mean of streamwise fluid force coefficient displays a smaller error: 0.21% for the same R_2/R_1 values, while between $y_{0'}$, f^*, and $C_{x'}$ the relative difference (for $R_2/R_1 = 200$ and 240) is under 0.04%. Comparing the results obtained for $R_2/R_1 = 240$ and 280, the relative difference for all of the investigate quantities is under 0.4%. For this reason, $R_2/R_1 = 240$ seems to be appropriate for the further systematic computations.

Second, a grid dependence study is carried out to analyze the influence of ξ_{max} (number of grid points in peripheral direction) on the results. $\xi_{max} = 300, 360$, and 420 are investigated, while the radius ratio and dimensionless time step values are fixed at $R_2/R_1 = 240$ and $\Delta t = 0.0004$, respectively. To generate an equidistant grid on the computational domain, η_{max} is varied with ξ_{max}; $\eta_{max} = 262, 314$, and 366 are used. The results of the grid dependence test are shown

Table 1
Effect of radius ratio on the computational results for $(Re, U^*, m^*, \zeta) = (300, 4.65, 10, 0\%)$.

R_2/R_1	$y_{0'}$	f^*	$C_{y'}$	$\overline{C}_x$	$C_{x'}$
200	0.3961	0.2135	0.2080	2.0158	0.6497
240	0.3962	0.2134	0.2111	2.0112	0.6498
280	0.3962	0.2134	0.2120	2.0094	0.6498

Table 2
Results of grid dependence study for $(Re, U^*, m^*, \zeta) = (300, 4.65, 10, 0\%)$.

ξ_{max}	$y_{0'}$	f^*	$C_{y'}$	$\overline{C}_x$	$C_{x'}$
300	0.3963	0.2135	0.2065	2.0156	0.6486
360	0.3962	0.2134	0.2111	2.0112	0.6498
420	0.3962	0.2134	0.2125	2.0103	0.6504

Table 3
Effect of dimensionless time step for $(Re, U^*, m^*, \zeta) = (300, 4.65, 10, 0\%)$.

Δt	$y_{0'}$	f^*	$C_{y'}$	$\overline{C}_x$	$C_{x'}$
0.0008	0.3964	0.2134	0.2146	2.0102	0.6518
0.0004	0.3962	0.2134	0.2111	2.0112	0.6498
0.0002	0.3962	0.2134	0.2097	2.0112	0.6489

in Table 2. Similarly to the data included in Table 1, $C_{y'}$ shows the highest relative difference: 2.18% for $\xi_{max} = 300$ and 360. As seen, the relative differences in $\overline{C}_x$ and $C_{x'}$ are smaller; 0.22% and 0.18%, respectively, when comparing the results at $\xi_{max} = 300$ and 360. Between $y_{0'}$ and f^* (also for $\xi_{max} = 300$ and 360), the relative difference does not exceed 0.05%. It is also shown in Table 2 that for $\xi_{max} = 360$ and 420 the relative difference between $y_{0'}, f^*, C_{y'}, \overline{C}_x$, and $C_{x'}$ is under 0.7%. Therefore, $\xi_{max} = 360$ seems to be adequate for further systematic simulations.

Finally, computations are carried out to test the dependence of computational results on the dimensionless time step. $\Delta t_1 = 2 \cdot 10^{-4} U^*$, $\Delta t_2 = 10^{-4} U^*$, and $\Delta t_3 = 5 \cdot 10^{-5} U^*$ time step values are considered. At the reduced velocity value applied in this particular independence study ($U^* = 4.65$), Δt_1, Δt_2, and Δt_3 are 0.0008, 0.0004, and 0.0002, respectively. The radius ratio and grid resolution values are fixed at $R_2/R_1 = 240$ and $\xi_{max} \times \eta_{max} = 360 \times 314$. The results are shown in Table 3. Again, the highest relative difference is observed in $C_{y'}$: 1.66% for Δt_1 and Δt_2, and 0.66% for Δt_2 and Δt_3. The errors in $C_{x'}$ are smaller: 0.31% when comparing the results for Δt_1 and Δt_2, and 0.1% for Δt_2 and Δt_3. It is also shown that the relative difference between $y_{0'}, f^*$, and $\overline{C}_x$ are negligible; these are under 0.05% for Δt_1 and Δt_2, and also for Δt_2 and Δt_3. Thus, the dimensionless time step value of $\Delta t = 10^{-4} U^*$ seems to be appropriate for further computations.

3.2. Validation

Validation is carried out using the previously determined computational parameters. Bourguet and Lo Jacono (2014) investigated undamped ($\zeta = 0\%$) transverse-only vortex-induced vibrations of a rotating cylinder at the Reynolds number and mass ratio values of $Re = 100$ and $m^* = 40/\pi$, respectively, using a numerical approach. Fig. 1 shows the dimensionless oscillation amplitude $\hat{y}_0$ against reduced velocity for a non-rotating cylinder. It can be seen that our results and those obtained by Bourguet and Lo Jacono (2014) compare well.

Blackburn and Henderson (1996) analyzed two-degree-of-freedom VIV of a circular cylinder by means of two-dimensional CFD computations. Reynolds number, mass ratio, and structural damping ratio values are fixed at $Re = 250$, $m^* = 40/\pi$, and $\zeta = 1\%$, respectively. Fig. 2a shows the dimensionless oscillation amplitude, and in Fig. 2b the non-dimensional vibration frequency normalized by the dimensionless vortex shedding frequency for a stationary cylinder (Strouhal number) f^*/St is shown against $(U^*St)^{-1}$. The calculation methodology of f^* is the same as that applied in Dorogi and Baranyi (2019); the dimensionless vibration frequency of the cylinder appears to be the highest intensity frequency peak in the FFT (Fast Fourier Transform) spectra of the non-dimensional cylinder displacement. It can be seen in Fig. 2 that the currently obtained results agree well with those presented in Blackburn and Henderson (1996). Note that higher discrepancies can be observed between $(U^*St)^{-1} \cong 1$ and 1.2 at the boundary of the lock-in domain where the solution depends highly on the reduced velocity.

Baranyi (2008) and Dorogi and Baranyi (2018, 2019) show further validation against numerical and experimental results available in the literature for both stationary and oscillating cylinder cases. All of these studies reported good agreement.

4. Results and discussion

As mentioned in Section 1, the vortex-induced vibration shows very different features at high and low Reynolds numbers. For high-*Re* cases, depending on the combined mass-damping parameter $m^*\zeta$ and also on the Reynolds number, two and three-branch responses can be found. In contrast, in the low-Reynolds-number domain, independently of $m^*\zeta$, only two-branch cylinder response has been identified; an upper branch has not yet been observed.

The main objective of this study is twofold; first, to investigate whether an upper branch (i.e. a three-branch cylinder response) can exist in the low-*Re* domain, and second, to analyze the effect of structural damping ratio on the cylinder response. For these aims, systematic CFD computations are carried out at fixed Reynolds number and mass ratio values of $Re = 300$ and $m^* = 10$, respectively. Damping ratio between $\zeta = 0\%$ and 5% is considered, that is, the combined mass-damping parameter is chosen to be in the range of $m^*\zeta = 0$ and 0.5. Reduced velocity based on the natural frequency of the cylinder in vacuum is varied from $U^* = 2.5$ to 7.5.

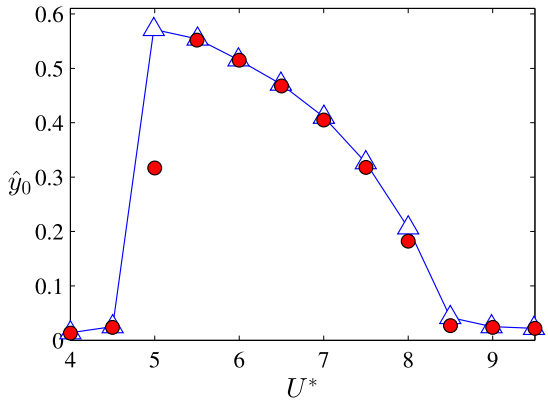

Fig. 1. Transverse-only vibration results: dimensionless oscillation amplitude $\hat{y}_0$ against U^* for $(Re, m^*, \zeta) = (100, 40/\pi, 0\%)$. ● Present study; △ Bourguet and Lo Jacono (2014).

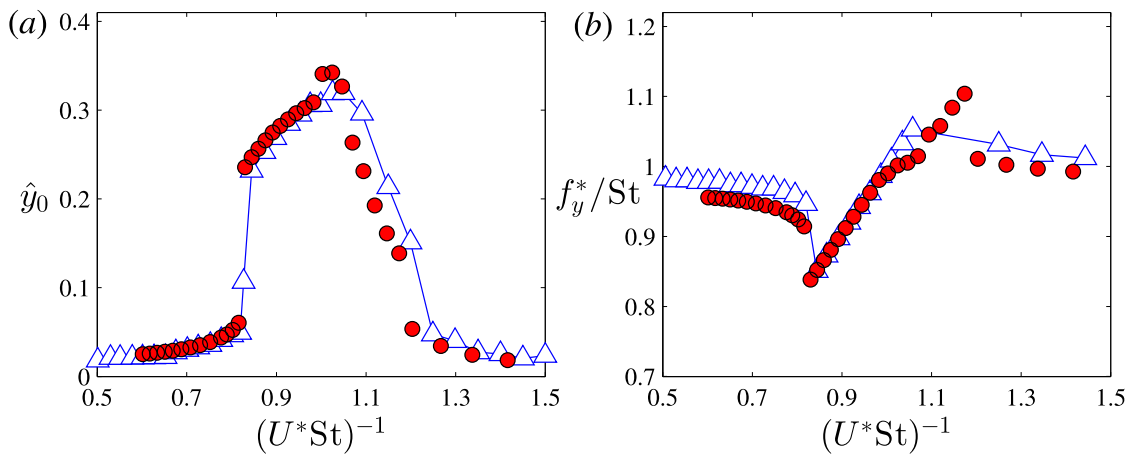

Fig. 2. Two-degree-of-freedom vibration results: dimensionless oscillation amplitude $\hat{y}_0$ (a) and non-dimensional vibration frequency normalized by the Strouhal number f^*/St (b) against $(U^*St)^{-1}$ for $(Re, m^*, \zeta) = (250, 40/\pi, 1\%)$. ● Present study; △ Blackburn and Henderson (1996).

Fig. 3a shows the root-mean square (rms) values of non-dimensional cylinder displacement $y_{0'}$, and in Fig. 3b the vibration frequency normalized by the cylinder's natural frequency in vacuum f/f_N is plotted against U^* for $\zeta = 0\%$. Similarly to that presented in Section 3.2, the oscillation frequency is calculated using the Fast Fourier Transform (see also Dorogi and Baranyi, 2019). The dashed line in Fig. 3b represents f_{v0}/f_N, where f_{v0} is the vortex shedding frequency for a stationary cylinder. The different response branches, namely the initial branch (*IB*), the upper branch (*UB*), and the lower branch (*LB*) identified in this study are shaded in different colors. It can be seen in Fig. 3 that in the range of $2.5 \leq U^* \leq 3.5$ the oscillation amplitude is low and the vibration frequency is close to the vortex shedding frequency for a stationary cylinder ($f \cong f_{v0}$). From $U^* = 3.5$ to 4 an initial branch is identified, where f/f_N represents an approximately constant value of $f/f_N \cong 0.95$ and $y_{0'}$ increases intensively.

Between $U^* = 4$ and 5.9 *lock-in* or *synchronization* is observed, where the vibration frequency locks to approximately the natural frequency of the cylinder (see Fig. 3b). The entire lock-in domain can be divided into two subdomains. Relatively high oscillation amplitudes are observed in the range of $4 < U^* \leq 4.89$ (see Fig. 3a), where the vibration frequency is slightly lower than the cylinder's natural frequency ($f/f_N < 1$, Fig. 3b). This reduced velocity domain appears to correspond to the upper branch. In order to confirm this, additional analyses are needed, which are presented in Section 4.1. At the higher boundary of the suggested upper branch $y_{0'}$ drops abruptly by 7%, and f passes through f_N. Govardhan and Williamson (2000) identified similar phenomena at the boundary separating upper and lower branches for $Re \cong 10^3 - 10^4$. Between $U^* = 4.89$ and 5.9 the lower branch is observed, where f is slightly higher than f_N (see Fig. 3b), and $y_{0'}$ reaches intermediate values (Fig. 3a). The reduced velocity range above $U^* = 5.9$ is out of the lock-in domain; the oscillation amplitude is low ($y_{0'} \cong 0.1$), and the vibration frequency is close again to the vortex shedding frequency for a stationary cylinder.

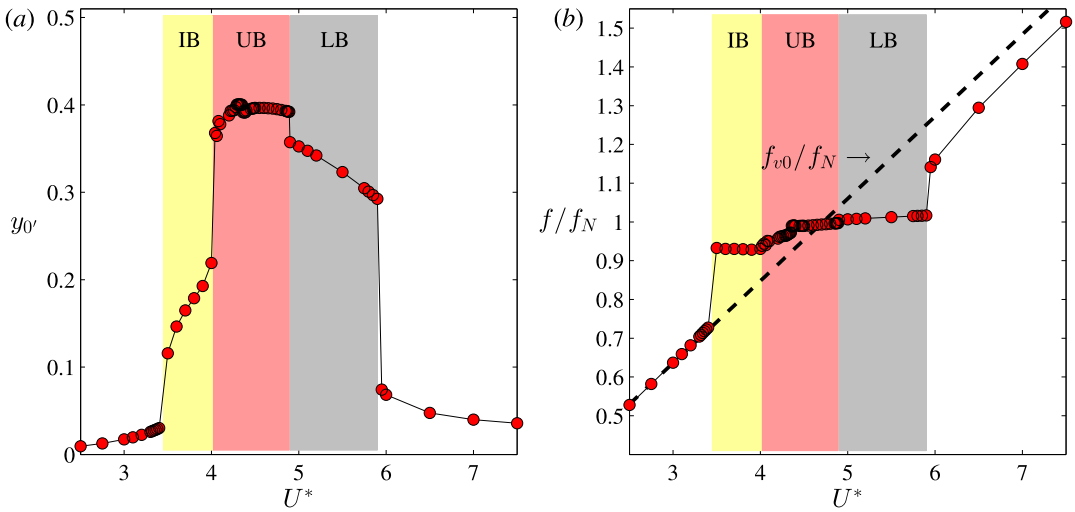

Fig. 3. Root-mean-square values of transverse cylinder displacements $y_{0'}$ (a) and vibration frequency normalized by the natural frequency of the cylinder in vacuum f/f_N (b) against reduced velocity for zero structural damping ratio $\zeta = 0\%$. Each response branch is shaded in a different color.

Govardhan and Williamson (2000), based on the methodology introduced by Lighthill (1986), applied the following decomposition on the instantaneous transverse fluid force F_y:

$$F_y = F_v + F_p. \tag{6}$$

In this formula F_v and F_p are the instantaneous vortex force and potential added mass force, respectively, per unit length of the cylinder. The potential added mass force is defined as follows (Govardhan and Williamson, 2000):

$$F_p = -C_A m_d \ddot{\tilde{y}}_0, \tag{7}$$

where C_A is the potential added mass coefficient, which is equal to unity for a circular cylinder (Blevins, 1990), $m_d = \rho \frac{d^2\pi}{4}$ is the displaced mass per unit length of the cylinder, and $\ddot{\tilde{y}}_0$ is the dimensional cylinder acceleration. Rearranging and normalizing Eq. (6) by $\frac{1}{2}\rho U_\infty^2 d$, the following expression can be obtained for the instantaneous vortex force coefficient:

$$C_v = C_y + \frac{\pi}{2}\ddot{y}_0, \tag{8}$$

where $\ddot{y}_0 = \frac{d}{U_\infty^2}\ddot{\tilde{y}}_0$ is the non-dimensional cylinder acceleration.

Fig. 4a and b show the rms values of transverse fluid force and vortex force coefficients $C_{y'}$ and $C_{v'}$, respectively, against U^* for $\zeta = 0\%$. It can be seen that for low cylinder displacements, i.e. in the domains of $2.5 \leq U^* \leq 3.45$ and $5.9 < U^* \leq 7.5$, $C_{y'}$ and $C_{v'}$ are approximately identical and near the value obtained for a stationary cylinder ($C_{y'} \cong C_{v'} \sim 0.5$, see Norberg, 2003). Govardhan and Williamson (2000) found $C_{y'} \cong C_{v'} \cong 0.1$ in the very low oscillation amplitude range (in $U^* < 4$ and $U^* > 10.5$ in their study), which is close to $C_{y'} \cong 0.05$, the value identified for a non-oscillating cylinder at $Re \sim 10^3$ (Norberg, 2003). In this sense, the currently obtained CFD results for $Re = 300$ and the experimental findings of Govardhan and Williamson (2000) for high Reynolds numbers show good qualitative agreement.

Increasing the reduced velocity in the initial branch, $C_{y'}$ increases gradually, and reaches its peak value at the beginning of the suggested upper branch (at $U^* = 4$, see Fig. 4a). Between $U^* = 4$ and 4.89 $C_{y'}$ drops dramatically, moreover at $U^* = 4.36$ (in the middle of the proposed upper branch) it suffers a sudden change from $C_{y'} \cong 0.71$ to approximately 0.25. It is also seen in Fig. 4a that at $U^* = 4.89$ $C_{y'}$ shows another but much smaller jump, above which it increases. The experimental results of Govardhan and Williamson (2000) and the above-mentioned tendencies in the current results are very similar. However, an abrupt change in $C_{y'}$ in the middle of the upper branch has not been identified in the high-Reynolds-number domain; this jump may indicate other important flow phenomena.

The rms values of vortex force coefficient (see Fig. 4b) found to decrease in the initial branch until it reaches its minimum value. The locations of the extreme values in $C_{y'}$ and $C_{v'}$ are near to each other. In the proposed upper branch $C_{v'}$ strongly increases, and at $U^* = 4.36$ (the corresponding reduced velocity value where $C_{y'}$ showed to jump) $C_{v'}$ changes suddenly between $C_{v'} \cong 0.53$ and 1.02. Similarly again to the tendencies observed in $C_{y'}$, at $U^* = 4.89$ $C_{v'}$ shows another but much smaller jump. The peak value in $C_{v'}$ is observed at the beginning of the lower branch, which qualitatively agrees well with the finding of Govardhan and Williamson (2000).

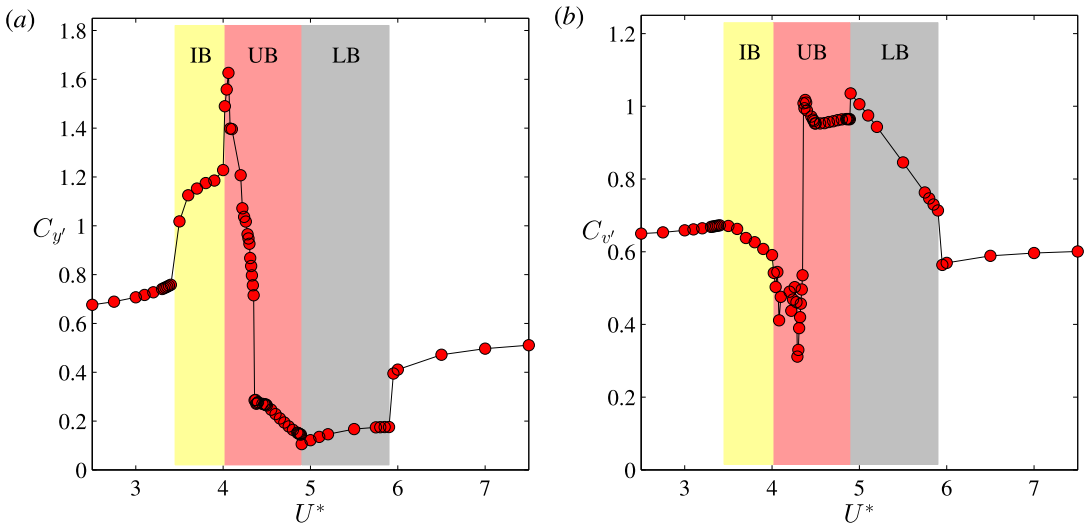

Fig. 4. Root-mean-square values of transverse fluid force coefficient $C_{y'}$ (a) and vortex force coefficient $C_{v'}$ (b) against reduced velocity for $\zeta = 0\%$. Each response branch is shaded in a different color.

4.1. Phase dynamics for undamped vibrations

The results presented earlier show that the upper branch most likely exists at the Reynolds number of 300. In order to confirm this proposal, additional analyses are required. Vortex-induced vibration of a circular cylinder is commonly investigated analytically using the harmonic oscillator model (Govardhan and Williamson, 2000). Let us assume that the motion of the cylinder and the aerodynamics force coefficients are sinusoidal functions of time:

$$y_0(t) = \hat{y}_0 \sin 2\pi f^* t, \tag{9}$$

$$C_y(t) = \hat{C}_y \sin(2\pi f^* t + \Phi), \tag{10}$$

$$C_v(t) = \hat{C}_v \sin(2\pi f^* t + \Phi_v), \tag{11}$$

where the hat symbol $(.\hat{}.)$ refers to amplitude. In these formulæ $\hat{C}_y$ and $\hat{C}_v$ are the amplitude of the transverse fluid force and vortex force coefficients, and $\hat{y}_0$ and f^* are the non-dimensional oscillation amplitude and frequency values. In these expressions Φ and Φ_v are the phase differences (or phase angles) for transverse fluid force and vortex force, respectively, relative to the cylinder displacement. For the sake of simplicity, Φ and Φ_v will be referred to as the *transverse* and *vortex phases*, respectively. Substituting Eqs. (9) and (10) into the cylinder equation of motion (see Eq. (1)), and equating the coefficients of sine and cosine terms, the following expressions can be obtained:

$$\cos\Phi = 2\pi^3 \frac{m^* \hat{y}_0}{\hat{C}_y U^{*2}} (1 - f^{*2} U^{*2}), \tag{12}$$

$$\sin\Phi = 4\pi^3 \frac{m^* \zeta \hat{y}_0}{\hat{C}_y U^*} f^*. \tag{13}$$

It can be seen in Eq. (13) that for zero structural damping, $\sin\Phi = 0$; therefore, the cylinder motion can only be in-phase ($\Phi = 0°$) or out-of-phase ($\Phi = 180°$) with the transverse fluid force. Eq. (12) shows that the transverse phase changes abruptly between $\Phi = 0°$ and $180°$ at the boundary where the vibration frequency passes through the natural frequency of the cylinder in vacuum, i.e. at $f^* U^* = 1$.

Introducing Eqs. (8), (9), and (11) into Eq. (1), and equating the coefficients of sine and cosine functions, the following formulæ are obtained:

$$\cos\Phi_v = 2\pi^3 \frac{(m^* + C_A)\hat{y}_0}{\hat{C}_v U_A^{*2}} (1 - f^{*2} U_A^{*2}), \tag{14}$$

$$\sin\Phi_v = 4\pi^3 \frac{\sqrt{m^*(m^* + C_A)}\zeta \hat{y}_0}{\hat{C}_v U_A^*} f^*, \tag{15}$$

where $U_A^* = U_\infty/(f_{N,a} d)$ is the reduced velocity based on the cylinder's natural frequency in still fluid $f_{N,a}$. Eq. (15) indicates that for undamped vibrations the cylinder displacement can only be in-phase or out-of-phase with the vortex force, similar

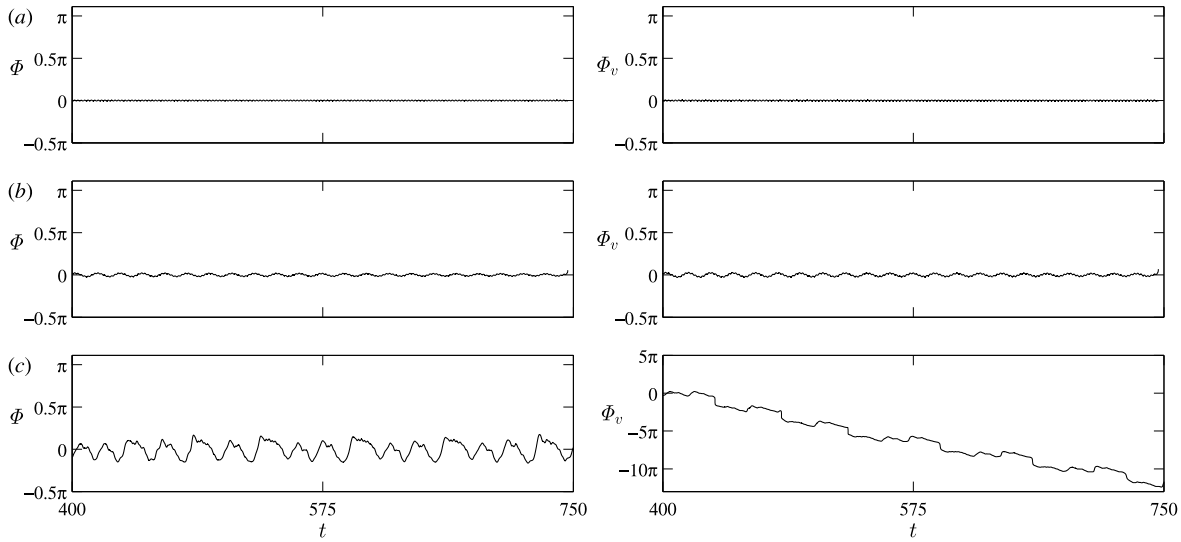

Fig. 5. Time histories of transverse phase Φ (left) and vortex phase Φ_v (right) at reduced velocity values of $U^* = 3$ (a) and 3.36 (b) corresponding to the very low amplitude range, and at $U^* = 4$ (c) in the initial branch for $\zeta = 0\%$.

to Φ, as shown earlier. As can be seen in Eq. (14), Φ_v changes suddenly between 0° and 180° at $f^* U_A^* = 1$, i.e. at the point where f crosses $f_{N,a}$.

Govardhan and Williamson (2000) carried out an experimental study at high Reynolds numbers [$Re = O(10^3 - 10^4)$] and low mass and damping values. They found that Φ_v and Φ jump at different reduced velocity values. The U^* domain which is enclosed between the two phase jumps (in Φ_v at its beginning, and in Φ at its higher boundary) corresponds to the frequently mentioned upper branch. In other words, to confirm that the range of $4 < U^* \leq 4.89$, where relatively high oscillation amplitudes are found, represents the upper branch, Φ and Φ_v should be investigated.

Pikovsky et al. (2001) defined phase angle as the phase difference between the displacement and the force. For the sake of comparison, we defined phase angles such that $\Phi = \Phi_{C_y} - \Phi_{y_0}$ and $\Phi_v = \Phi_{C_v} - \Phi_{y_0}$. In these expressions Φ_{C_y}, Φ_{C_v}, and Φ_{y_0} are the time-dependent phases of C_y, C_v, and y_0, respectively, which are computed using the Hilbert transform of the corresponding signals (Khalak and Williamson, 1999; Pikovsky et al., 2001; Konstantinidis et al., 2020). In the figures mostly time-dependent phase differences (Φ and Φ_v) are plotted in radian as unwrapped signals. However, their time-average values ($\overline{\Phi}$ and $\overline{\Phi}_v$) are shown in degrees, and are calculated via averaging Φ and Φ_v wrapped in $[-\pi/2, 3\pi/2]$.

Fig. 5 shows Φ (on the left-hand side) and Φ_v (right) for different reduced velocity values in the very low amplitude range (see Fig. 5a and b) and in the initial branch (Fig. 5c). It can be seen that in the domain of $2.5 \leq U^* \leq 3.45$ transverse and vortex phases are approximately constant; only small oscillations are observed near $U^* = 3.45$ (Fig. 5b). In the initial branch ($3.45 < U^* \leq 4$) Φ shows intermediate oscillations, but its time-mean value is roughly zero (Fig. 5c). However, in the same range Φ_v shows an unbounded decrease, which corresponds to the loss of synchronization between cylinder motion and the vortex force coefficient (Pikovsky et al., 2001). Konstantinidis et al. (2020) found an unbounded change (increase) in the time-dependent transverse phase Φ in the second half of the upper branch at high Reynolds numbers. In Pikovsky et al. (2001) this phenomenon is interpreted by analyzing the relationship between motion and forcing frequencies.

In Fig. 6 differences of vibration frequency relative to the frequency of transverse fluid force and vortex force coefficients, i.e. $f^* - f^*_{C_y}$ and $f^* - f^*_{C_v}$, respectively, are shown against U^* in the initial, proposed upper, and lower branches. These quantities are called detuning. It can be seen that in the initial branch $f^* > f^*_{C_v}$, which explains why the time-dependent vortex phase decreases in this domain (Pikovsky et al., 2001). In addition, the difference between the two frequency values is relatively large in this range ($3.45 < U^* \leq 4$), which causes the roughly uniform drop in the vortex phase (see Fig. 5c). It is also shown in Fig. 6 that $f^* - f^*_{C_y} \cong 0$ in the initial branch, which implies the roughly constant value of transverse phase.

Based on Fig. 3, the upper branch is expected to appear in the domain of $4 < U^* \leq 4.89$. This reduced velocity range comprises five subregions with (slightly) different characteristics, which are denoted by $UB(I)$, $UB(II)$, $UB(III)$, $UB(IV)$, and $UB(V)$. These regimes will be detailed in the following part of this study. Fig. 7a and b show the times histories of transverse and vortex phases in $UB(I)$, which covers the domain of $4 < U^* \leq 4.28$. In contrast to the trends observed in the initial branch, in $UB(I)$ f^* is lower than $f^*_{C_v}$ (see Fig. 6), which leads to increasing Φ_v (Fig. 7). It can also be seen in Fig. 6 that $|f^* - f^*_{C_v}|$ is significantly lower in $UB(I)$ compared to that in the initial branch. Pikovsky et al. (2001) found that when the value of detuning decreases, the time history of the phase difference changes remarkably. As shown in Fig. 7,

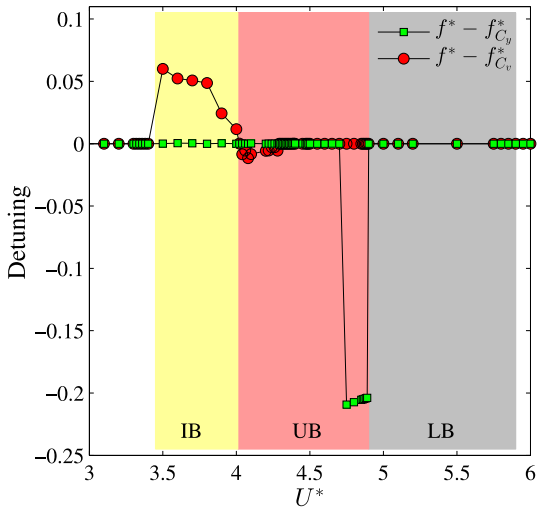

Fig. 6. Detuning values $f^* - f^*_{C_y}$ and $f^* - f^*_{C_v}$ against reduced velocity in the initial, upper, and lower branches for $\zeta = 0\%$. Here f^*, $f^*_{C_y}$, and $f^*_{C_y}$ are the frequency values of cylinder displacement, transverse fluid force, and vortex force coefficients, respectively. Each response branch is shaded in a different color.

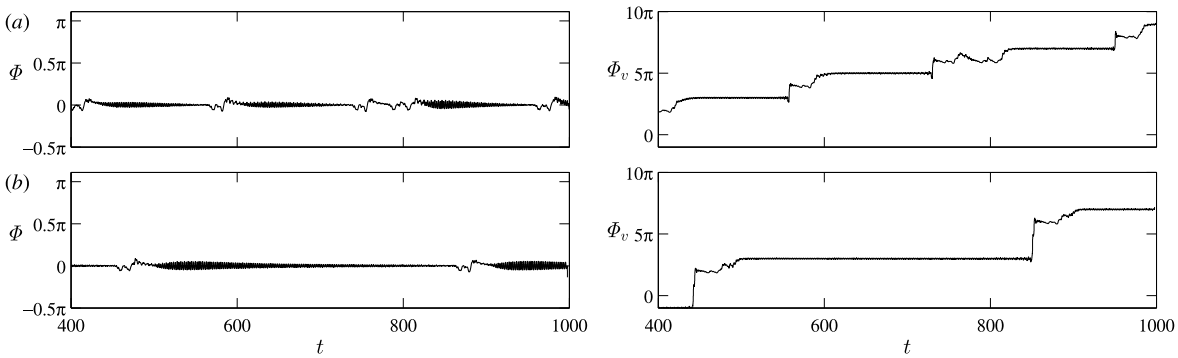

Fig. 7. Time histories of transverse phase Φ (left) and vortex phase Φ_v (right) at $U^* = 4.2$ (a) and 4.28 (b) in $UB(I)$ for $\zeta = 0\%$.

instead of unbounded growth, Φ_v consists of time intervals, so called *epochs* (Pikovsky et al., 2001), where the vortex phase is approximately constant. It can be observed that the time length of an epoch extends with the reduced velocity. Two neighboring epochs are separated by so-called *phase slips*, where the vortex phase shows rapid change (Pikovsky et al., 2001). Konstantinidis et al. (2020) identified similar tendencies (i.e. epochs separated by phase slips) in the time-dependent transverse phase close to the boundary between the upper and lower branches. In addition, Fig. 7a and b show "approximately constant" Φ values, which is expected because $|f^* - f^*_{C_y}| \cong 0$ in $UB(I)$ (Fig. 6). Note that in this context, the phrase "approximately constant" refers to that the phase difference varies around a constant value (in this case around zero).

Fig. 8 shows the time histories of vortex phase wrapped between $-\pi/2$ and $3\pi/2$ at different reduced velocity values corresponding to the initial branch (Fig. 8a) and the onset of proposed upper branch ($UB(I)$, see Fig. 8b and c). Pikovsky et al. (2001) showed that the change of Φ_v via a phase slip (see Fig. 7) cannot be arbitrary, it is always the whole number multiples of π. This finding is confirmed in Fig. 8b and c. It is also important to see that at an epoch Φ_v varies periodically around π (see Fig. 8a and b), and Φ represents an almost constant zero value (Fig. 7). For this reason, conditions for the existence of the upper branch ($\Phi_v = \pi$ and $\Phi = 0$) seem to be satisfied in $UB(I)$. However, in-between two epochs (in phase slips) vortex phase deviates marginally from π, which causes discrepancies in its time-mean value. As shown before, time lengths of epochs increase with U^*, that is, deviation in $\overline{\Phi}_v$ from its theoretically expected value ($\overline{\Phi}_v = 180°$) decreases with reduced velocity. Similar issues appear in the initial branch (see Fig. 8a), where the wrapped phase angle shows high spikes that influences $\overline{\Phi}_v$ significantly. In further time-averaged phase difference plots, non-synchronous cases – where unbounded changes or phase slips are identified – will be indicated by empty symbols.

Fig. 9 shows the time histories of transverse and vortex phases in the remaining part of the upper branch. As can be seen in Fig. 6, the frequencies of vortex force and transverse fluid force are equal to the vibration frequency of the cylinder between $U^* = 4.28$ and 4.7. Consequently, "approximately constant" Φ and Φ_v values are expected in this

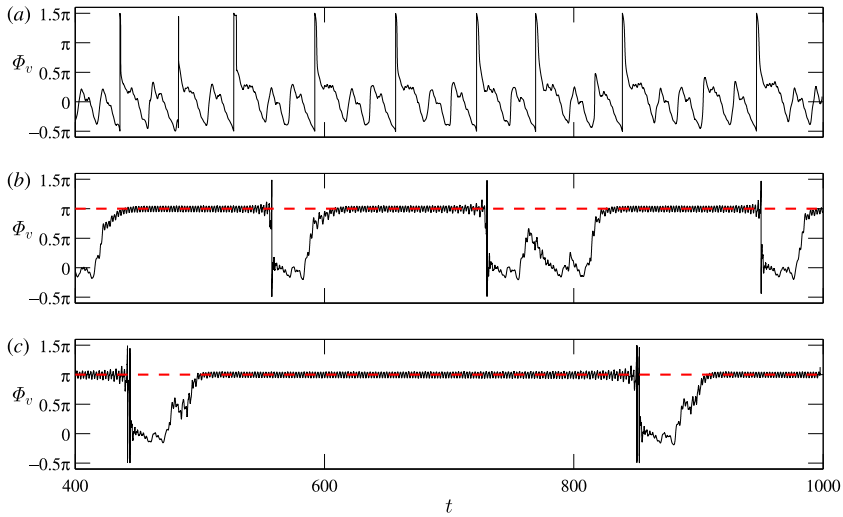

Fig. 8. Time-dependent vortex phase at $U^* = 4$ (a): initial branch, 4.2 (b): $UB(I)$, and 4.28 (c): $UB(I)$ for $\zeta = 0\%$. Here, phase difference is wrapped in $[-\pi/2; 3\pi/2]$.

domain. Fig. 9a–c corroborate these expectations: neither unbounded change nor phase slips are identified in Φ and Φ_v. It is also seen in these figures that the time-mean values of Φ_v and Φ equal approximately to π and 0, respectively, which are consistent with the experimental results for the upper branch. This finding strengthens our previous evidence concerning the existence of the upper branch at $Re = 300$.

It can also be observed in Fig. 9a–c that the fluctuations in transverse and vortex phases are amplified when U^* is increased. As can be seen, in $UB(II)$ ($4.28 < U^* \leq 4.35$), both Φ and Φ_v show small periodic oscillations (see Fig. 9a). Varying the reduced velocity in $UB(III)$ (from $U^* = 4.36$ to 4.48), Φ oscillates randomly with very high rms values (Fig. 9b). Random oscillations are also observed in the time history of Φ_v, but its fluctuation is significantly lower. Shifting to $UB(IV)$ (takes place in $4.48 < U^* \leq 4.7$), transverse and vortex phases return back to periodic, but the high fluctuations in Φ are still observed (see Fig. 9c).

Finally, increasing the reduced velocity through $UB(V)$ (in the range of $U^* = 4.7 - 4.89$), we found that detuning $f^* - f^*_{C_y}$ drops to approximately -0.2 (see Fig. 6), which causes an unbounded increase in the transverse phase (Fig. 9d). It is interesting to note that the absolute value of this detuning is close to the Strouhal number at $Re = 300$, i.e. $f^* - f^*_{C_y} \cong -St$. Besides, the vibration frequency is also close to St in $UB(V)$ ($f^* \cong St$, see Fig. 3b). Consequently, the detuning value of -0.2 can only be achieved when the frequency of transverse fluid force, more precisely, the most dominant frequency component in the spectra of C_y is double the frequency of cylinder oscillation, $f^*_{C_y} \cong f^* \cong 2St$. Moreover, the unreasonably high fluctuations in Φ in the $UB(III)$ and $UB(IV)$ subdomains appear to be caused by the occurrence of higher order harmonics in the spectra of C_y. These effects are further investigated in Section 4.4.

Fig. 10 shows Φ and Φ_v in the range of $4.89 < U^* \leq 5.9$, the domain corresponding to the lower branch, because $\overline{\Phi} \cong \overline{\Phi}_v \cong 180°$ (Govardhan and Williamson, 2000; Soti et al., 2018). It can be seen that the rms values of transverse and vortex phases decrease with reduced velocity.

Fig. 11 displays the time-mean values of transverse and vortex phases $\overline{\Phi}$ and $\overline{\Phi}_v$, respectively, in degrees, where filled and empty symbols indicate synchronous and non-synchronous cases. Although phase differences show gradual variations between 0° and 180°, the transitions in $\overline{\Phi}_v$ and $\overline{\Phi}$ are observed in different U^* ranges, which is the distinctive feature of three-branch response. However, experimental studies at high Reynolds numbers and low mass and damping values reported abrupt phase changes in the initial↔upper and upper↔lower branch transition domains. As discussed earlier, the reason behind the gradual and not abrupt variations in $\overline{\Phi}_v$ and $\overline{\Phi}$ is the unbounded changes and phase slips found in the time-dependent transverse and vortex phases.

To conclude, the initial branch is observed in the range of $3.45 < U^* \leq 4$, the upper branch between $U^* = 4$ and 4.89, and the lower branch in the domain of $4.89 < U^* \leq 5.9$. The most important observations related to the dynamics of Φ and Φ_v at the different response branches are summarized in Table 4.

4.2. Analysis for non-zero damping ratios

In this study the effect of structural damping ratio is also investigated. We would like to learn more about the effect of ζ on the cylinder response, particularly on the occurrence of upper branch. Fig. 12a and b show $y_{0'}$ and f/f_N against reduced velocity for damping ratio values between $\zeta = 0\%$ and 5%. It can be seen that the results obtained harmonize well with the expectations: the oscillation amplitude decreases with damping ratio (see Fig. 12a). It can also be clearly

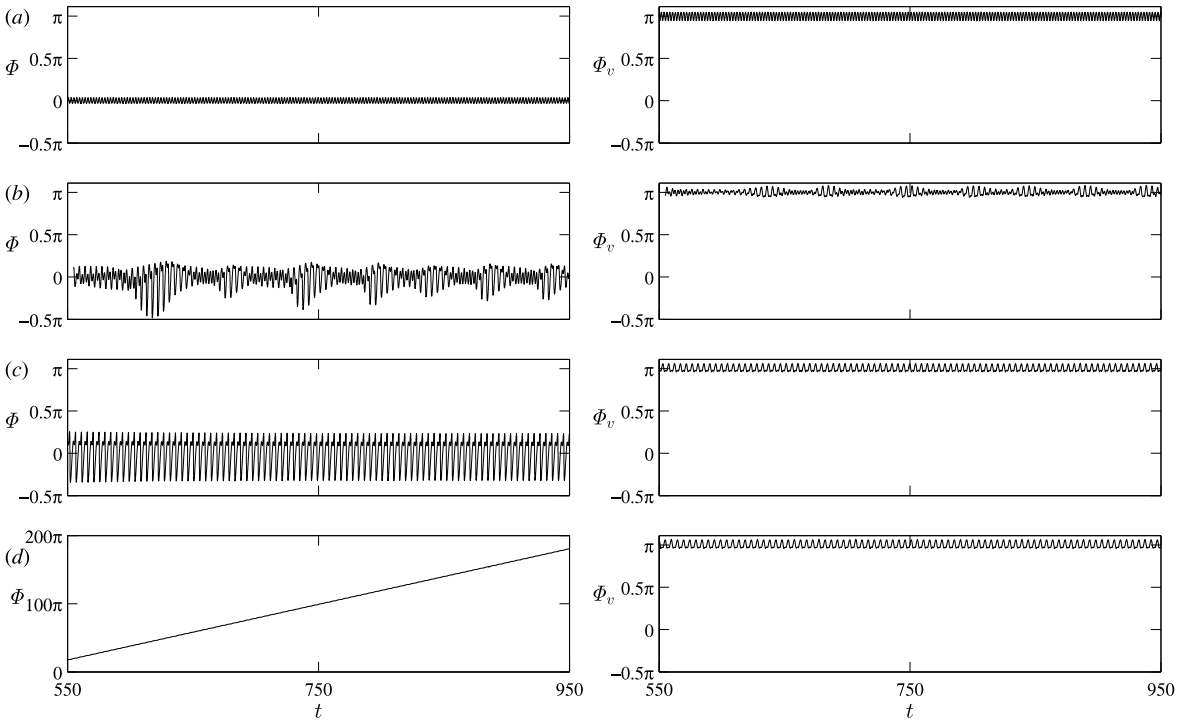

Fig. 9. Time-varying phase differences Φ (left) and Φ_v (right) at $U^* = 4.35$ (a): $UB(II)$, 4.4 (b): $UB(III)$, 4.65 (c): $UB(IV)$, and 4.89 (d): $UB(V)$ for $\zeta = 0\%$.

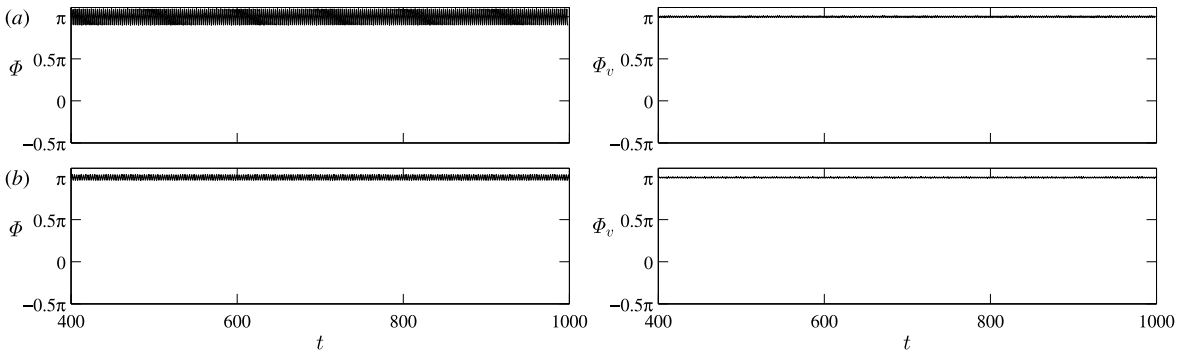

Fig. 10. Time-dependent phase differences Φ (left) and Φ_v (right) at $U^* = 4.9$ (a) and 5.5 (b) in the lower branch for $\zeta = 0\%$.

Table 4
Summary of phase dynamics in the three response branches.

Branch	Abbrev.	U^* domain	Φ	Φ_v
–	–	[2.50, 3.45]	Low periodic osc.	Low periodic osc.
Initial	IB	]3.45, 4.00]	Intermediate osc.	Unbounded decrease
Upper	$UB(I)$	]4.00, 4.28]	Low random osc.	Phase slips
	$UB(II)$	]4.28, 4.35]	Low periodic osc.	Low periodic osc.
	$UB(III)$	]4.35, 4.48]	High random osc.	Low random osc.
	$UB(IV)$	]4.48, 4.70]	High periodic osc.	Low periodic osc.
	$UB(V)$	]4.70, 4.89]	Unbounded increase	Low periodic osc.
Lower	LB	]4.89, 5.90]	Low periodic osc.	Low periodic osc.

observed that structural damping causes significant changes in the cylinder response. When the damping ratio is varied in the range of $\zeta = 0 - 1\%$, $y_{0'}$ and f/f_N curves are very similar to each other; they form a three-branch response. As seen in the figure, the beginning of the initial branch (where $y_{0'}$ starts to increase intensively) and the beginning of the lower

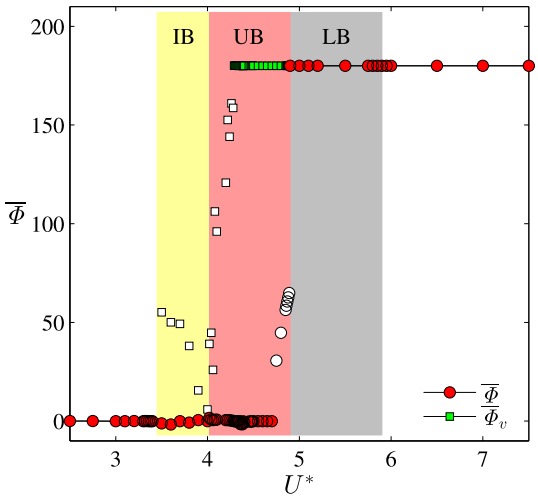

Fig. 11. Time-mean values transverse and vortex phases against U^* for $\zeta = 0\%$. Here synchronous and non-synchronous cases are denoted by filled and empty symbols, respectively. Each response branch is shaded in a different color.

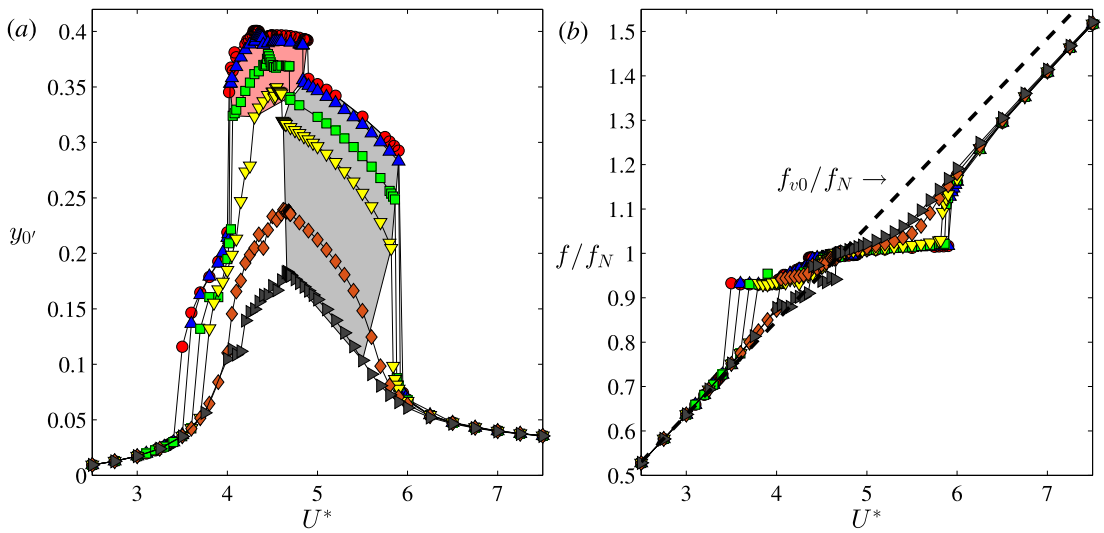

Fig. 12. Root-mean square values of transverse cylinder displacement $y_{0'}$ (a) and vibration frequency normalized by the natural frequency of the cylinder in vacuum f/f_N (b) against reduced velocity for $\zeta = 0\%$ (—●—), 0.1% (—▲—), 0.5% (—■—), 1% (—▽—), 3% (—◆—), and 5% (—▶—). The areas corresponding to upper and lower branch are shaded in red and gray, respectively. (For interpretation of the references to colour in this figure legend, the reader is referred to the web version of this article.)

branch (where $y_{0'}$ shows a sudden downward jump and f passes through f_N) depend strongly on the damping ratio; as we increase ζ, they shift to higher and lower U^* values, respectively. Klamo et al. (2006) showed somewhat different features, as in their study the upper↔lower branch transition range remained independent of the structural damping. Soti et al. (2018) investigated a wider ζ range, and showed that the boundary between the upper and lower branches occurred at lower U^* values when damping was increased.

Fig. 13 shows the time-dependent transverse and vortex phases in the initial branch (Fig. 13a), upper branch (Fig. 13b and Fig. 13c), and lower branch (Fig. 13d) for $\zeta = 0.5\%$. It can be seen in Fig. 13a that Φ_v shows an unbounded decrease in the initial branch, similar to that observed for undamped vibrations. At the beginning of the upper branch phase slips are found in the vortex phase (Fig. 13b), a tendency that is similar to that observed in the $UB(I)$ subdomain identified for $\zeta = 0\%$. However, interestingly, Φ_v remains "approximately constant", because the detuning $f^* - f^*_{C_v}$ is zero in this range. Increasing the reduced velocity in the further part of the upper branch, the results show similar features to those reported for $\zeta = 0\%$. However, the range where transverse phase displays an unbounded increase (i.e. the $UB(V)$ subdomain found for zero structural damping) seems to diminish with the structural damping ratio, and at $\zeta = 0.5\%$ it is not observed. Fig. 13c shows Φ and Φ_v in the upper branch, just before the jump to the lower branch, and here the transverse phase

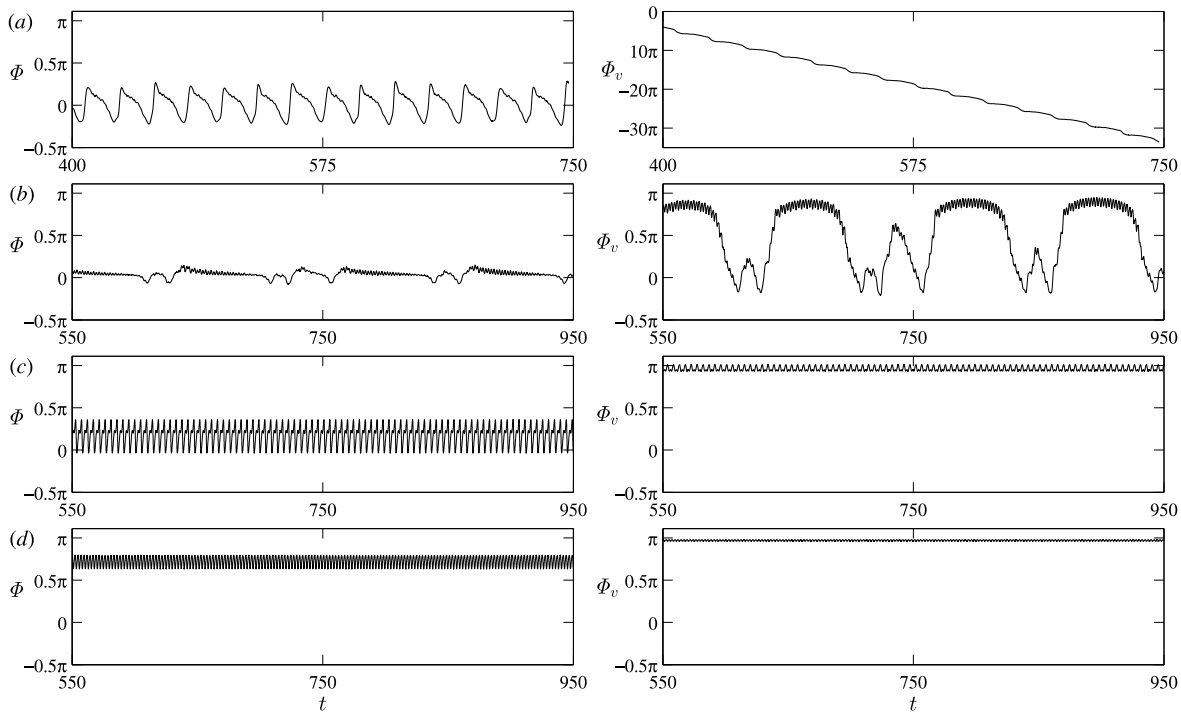

Fig. 13. Time histories of phase differences Φ (left) and Φ_v (right) at reduced velocity values of $U^* = 3.8$ (a), 4.25 (b), 4.68 (c), and 4.8 (d) for $\zeta = 0.5\%$.

is "approximately constant"; it does not show an unbounded increase. The possible reason behind this phenomenon is that the role of the second harmonic frequency component changes with the structural damping ratio. This effect will be further analyzed in Section 4.4.2.

It can also be seen in Fig. 12 that cylinder responses for $\zeta = 3\%$ and 5% are different from those for $\zeta = 0 - 1\%$. For these *high-damping cases* $y_{0'}$ and f/f_N show smooth variations; no sudden changes are identified in these quantities. Since the condition of $f/f_N \cong 1$ does not satisfy, no classic lock-in domains are found for high structural damping values. This is in contrast to the phenomenon observed for $\zeta \leq 1\%$. Although Prasanth et al. (2011) investigated the effect of mass ratio, they carried out CFD computations for $\zeta = 0.1\%$ and 10%. For $\zeta = 10\%$ they observed a similar phenomenon; f/f_N increased almost linearly with U^*. It is important to note that for $\zeta = 3\%$ and 5% and $Re = 300$, the upper branch does not occur, only initial and lower branches, namely two-branch responses are identified. Feng (1968), Khalak and Williamson (1999), Klamo et al. (2006), and Soti et al. (2018) found also that increasing the damping ratio (or the combined mass-damping parameter) can lead to the transition from three-branch to two-branch response. In order to show explicitly that upper branch does not occur for $\zeta = 3\%$ and 5%, transverse and vortex phases are analyzed.

As already discussed in Section 4.1, theoretically, the upper branch is characterized by abrupt phase jumps at its lower and higher boundaries. Although for zero damping ratio, phase difference values of 0° and 180° are the only theoretically possible values (as shown by Eqs. (13) and (15)), for $\zeta > 0\%$ $\overline{\Phi}$ and $\overline{\Phi}_v$ are allowed to vary between 0° and 180° (Leontini et al., 2006b). Fig. 14a and b show $\overline{\Phi}$ and $\overline{\Phi}_v$ against reduced velocity for different damping ratio values. Similarly to the notations employed in Fig. 11, filled and empty symbols refer to synchronous and non-synchronous cases. It can be seen in Fig. 14 that for relatively high cylinder displacements, time-averaged phase differences, especially $\overline{\Phi}$, depend on structural damping. Similarly to undamped vibrations, $\overline{\Phi}_v$ increases gradually at the initial↔upper branch transition range, while $\overline{\Phi}$ transitions at the boundary separating upper and lower branches. It is also seen in Fig. 14 that the change of $\overline{\Phi}_v$ through the initial↔upper branch transition range is a weak function of the damping ratio. For instance, for $\zeta = 0.1\%$ $\overline{\Phi}_v$ changes by 175.08° and for $\zeta = 1\%$ by 159.77°. However, the increment observed in $\overline{\Phi}$ depends strongly on ζ; for $\zeta = 0.1\%$ $\overline{\Phi}$ jumps roughly by 158.1° and for $\zeta = 1\%$ only by 43.4°. Moreover, for high structural damping cases (at $\zeta = 3\%$ or 5%) jumps in $\overline{\Phi}$ disappear, resulting in an almost continuous increase of the time-averaged phase angle. This finding compares qualitatively well with the experimental results of Soti et al. (2018).

In Table 5 we compare the currently obtained computational results for $Re = 300$ with the high-Reynolds-number experimental results presented in Klamo et al. (2006) and Soti et al. (2018). This table involves the mass ratio values, the Reynolds numbers at the peak oscillation amplitude points $Re(\hat{y}_{0max})$, the lower limits of upper and lower branches U^*_{UB} and U^*_{LB}, and the widths of the upper branch $\Delta U^* = U^*_{UB} - U^*_{LB}$. Note that in Table 5 U^*_{UB}, U^*_{LB}, and ΔU^* are reduced velocity values based on the cylinder's natural frequency in vacuum f_N. However, Klamo et al. (2006) and Soti et al. (2018) defined

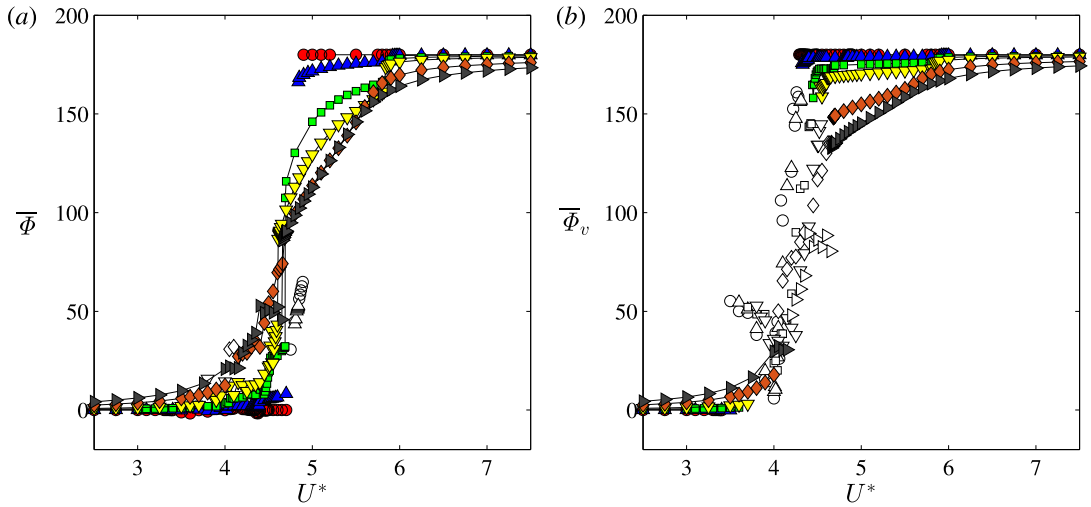

Fig. 14. Time-mean values of transverse $\overline{\Phi}$ (a) and vortex phases $\overline{\Phi}_v$ (b) against reduced velocity for different ζ values for $\zeta = 0\%$ (—●—), 0.1% (—▲—), 0.5% (—■—), 1% (—▼—), 3% (—◆—), and 5% (—▶—). Filled and empty symbols refer to synchronous and non-synchronous cases, respectively. (For interpretation of the references to colour in this figure legend, the reader is referred to the web version of this article.)

Table 5
Effect of damping ratio on cylinder response compared to the experimental data in Klamo et al. (2006) and Soti et al. (2018). Here U^*_{UB} and U^*_{LB} are the reduced velocity values where cylinder response shifts to upper and lower branches, respectively, and ΔU^* is the width of the upper branch.

Present study $m^* = 10$, $Re = 300$				Klamo et al. (2006) $m^* = 78.3$, $Re(\hat{y}_{0max}) \cong 1000$				Soti et al. (2018) $m^* = 3$, $Re(\hat{y}_{0max}) \cong 3200$			
$m^*\zeta$	U^*_{UB}	U^*_{LB}	ΔU^*	$m^*\zeta$	U^*_{UB}	U^*_{LB}	ΔU^*	$m^*\zeta$	U^*_{UB}	U^*_{LB}	ΔU^*
0.00	4.00	4.89	0.88	–	–	–	–	–	–	–	–
0.01	4.03	4.84	0.80	–	–	–	–	0.015	4.16	6.42	2.26
0.05	4.06	4.69	0.63	0.047	4.97	5.66	0.69	0.060	4.31	6.24	1.93
0.10	4.30	4.61	0.31	0.120	5.21	5.65	0.44	0.110	4.50	6.23	1.73
0.30	–	4.68	–	–	–	–	–	0.370	4.67	5.89	1.22
0.50	–	4.66	–	–	–	–	–	0.500	4.49	5.53	1.04

reduced velocity based on natural frequency in still fluid $f_{N,a}$. In order to convert between the two U^* values (based on f_N and $f_{N,a}$) the following approximate relationship is used:

$$\frac{U_\infty}{f_N d} \cong \frac{U_\infty}{f_{N,a} d}\sqrt{\frac{m^*}{m^*+1}}. \tag{16}$$

It can be seen in Table 5 that our computational results and the experimental data in Klamo et al. (2006) and Soti et al. (2018) show similar trends; as we increase the damping ratio, the U^* range of the upper branch diminishes. The currently obtained CFD results show that upper branch completely disappears before reaching the damping ratio value of 3%; for $\zeta = 3\%$ and 5% only initial and lower branches remain. In other words, for low-damping cases ($0\% \le \zeta \le 1\%$) three-branch responses are identified, and for high-damping cases (at $\zeta = 3\%$ and 5%) two-branch responses are found.

Surprisingly, the width of the upper branch obtained in this study agrees relatively well with the data presented in Klamo et al. (2006). However, Soti et al. (2018) found much larger ΔU^* values; for example at $m^*\zeta = 0.11$ they showed $\Delta U^* \cong 1.7$, which is almost four times larger than the value obtained by Klamo et al. (2006) at approximately the same mass-damping value ($m^*\zeta \cong 0.12$). Govardhan and Williamson (2006) and Klamo et al. (2006) found that the Reynolds number strongly influences the cylinder response. Table 5 shows that in Klamo et al. (2006) the Reynolds number at the peak oscillation amplitude point $Re(\hat{y}_{0max}) \cong 1000$ is relatively close to $Re = 300$ employed in this study, while in Soti et al. (2018) $Re(\hat{y}_{0max})$ was much larger [$Re(\hat{y}_{0max}) \cong 3200$]. This observation may explain why the currently obtained ΔU^* values shows better agreement with Klamo et al. (2006)'s data than with those in Soti et al. (2018).

4.3. Mechanical energy transfer and peak vibration amplitudes

The non-dimensional mechanical energy transferred between the oscillating cylinder and the surrounding fluid is defined as follows (Blackburn and Henderson, 1999; Baranyi, 2008):

$$E = \frac{1}{n}\int_0^{nT} C_y(t)\dot{y}_0(t)\mathrm{d}t, \tag{17}$$

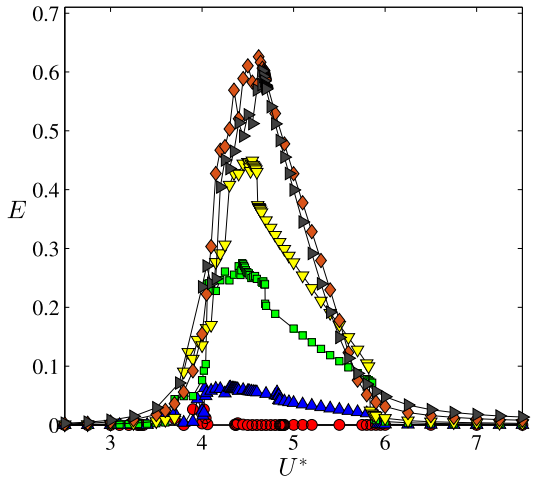

Fig. 15. Mechanical energy transfer against reduced velocity for $\zeta = 0\%$ (—●—), 0.1% (—▲—), 0.5% (—■—), 1% (—▼—), 3% (—◆—), and 5% (—▶—). (For interpretation of the references to colour in this figure legend, the reader is referred to the web version of this article.)

where T is the motion period and n is the number of oscillation cycles taken into account when evaluating the integral above. In this study mostly $n = 100$ is used for calculation of the mechanical energy transfer.

Using the harmonic assumptions introduced by Eqs. (9)–(11), E can be expressed as follows (Jauvtis and Williamson, 2004; Bernitsas et al., 2008; Tang et al., 2017):

$$E = \pi \hat{y}_0 \hat{C}_y \sin \Phi. \tag{18}$$

Multiplying the equation of cylinder motion (see Eq. (1)) by the instantaneous velocity of the cylinder, and integrating it over one cycle of cylinder oscillation, the following expression is obtained also for the mechanical energy transfer:

$$E = 4\pi^4 \hat{y}_0^2 f^* U^{*-1} m^* \zeta. \tag{19}$$

Bernitsas et al. (2008) derived the power transfer between the oscillating cylinder and the surrounding fluid, which is analogous with Eq. (19). Fig. 15 shows E (calculated based on Eq. (17)) against reduced velocity for different damping ratio values. It can be seen that the mechanical energy transfer is approximately zero for undamped cylinder vibrations. Eqs. (18) and (19) verify this finding; zero energy transfer can only be achieved when the transverse fluid force is in-phase or out-of-phase with the cylinder displacement ($\Phi = 0°$ and $180°$), i.e. for $\zeta = 0\%$ (see Fig. 14). However, in the initial branch and at the beginning of the upper branch E shows low but non-zero values; these errors can be explained by the quasi-periodic nature of signals. It was shown earlier that for $\zeta > 0\%$, the time-mean values of transverse and vortex phases vary between 0° and 180° (Fig. 14), which implies $E > 0$ (see Eq. (19)). Fig. 15 shows exactly the same: for positive damping, E is always positive. Note that positive E means that the energy is transferred from the fluid to the cylinder. It can also be seen in Fig. 15 that increasing damping ratio up to $\zeta = 3\%$ the energy transfer curves shift upwards. Since $y_{0'}$ is very low at $\zeta = 3\%$ and 5% (Fig. 12), energy transfer cannot further increase; thus, there is a negligible difference between E values obtained for $\zeta = 3\%$ and 5%. Soti et al. (2018) carried out a large number of experiments for high Re analyzing the effects of damping ratio. Based on the displacement of the cylinder and the aerodynamic forces they evaluated the power transfer which is proportional to E. They found also that the power (and energy) transfer can be magnified by applying higher structural damping.

Equating Eqs. (18) and (19) the following formula is obtained (Morse and Williamson, 2009):

$$\hat{C}_y \sin \Phi = 4\pi^3 f^* U^{*-1} m^* \zeta \hat{y}_0. \tag{20}$$

Vandiver (2012) introduced dimensionless damping $c^* = 4\pi c f/(\rho U_\infty^2)$, which appears in Eq. (20) as $c^* = 4\pi^3 f^* U^{*-1} m^* \zeta$. For this reason, the relationship between the excitation force coefficient $\hat{C}_y \sin \Phi$ and the oscillation amplitude can be written simply as:

$$\hat{C}_y \sin \Phi = c^* \hat{y}_0. \tag{21}$$

In the experimental results of Lee and Bernitsas (2011) the maximum excitation force coefficient was $\hat{C}_y \sin \Phi \cong 0.79$. Substituting this value into Eq. (21), Vandiver (2012) obtained $\hat{y}_{0max} = 0.79/c^*$ for the peak oscillation amplitude. Based on the total energy balance, Konstantinidis (2013) reconsidered c^*, and created the formula of $\hat{y}_{0max} = k_c/\sqrt{c^*}$ describing also the peak oscillation amplitude. He suggested k_c in the range of $k_c = 0.46 - 0.78$. Konstantinidis (2013) compared his and Vandiver (2012)'s empirical relationship with the experimental data of Lee and Bernitsas (2011). He found that $\hat{y}_{0max} = 0.79/\sqrt{c^*}$ estimates the peak amplitude data well in a wider c^* range.

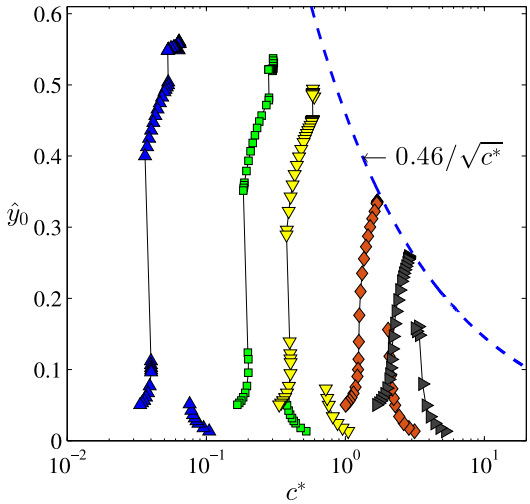

Fig. 16. Dimensionless oscillation amplitude against nondimensional damping for $\zeta = 0.1\%$ (—▲—), 0.5% (—■—), 1% (—▽—), 3% (—◆—), and 5% (—▶—). Blue dashed line represents the peak oscillation amplitude approximated by Konstantinidis (2013). (For interpretation of the references to colour in this figure legend, the reader is referred to the web version of this article.)

Table 6
Comparison of the peak vibration amplitude values for undamped cylinder vibrations at the low–*Re* domain.

Citation	DoF	*Re*	m^*	$\hat{y}_{0max}$
Zhang et al. (2015)	1	60	50	0.509
Shiels et al. (2001)	1	100	0	0.580
Shen et al. (2009)	1	100	$10/\pi$	0.570
Bourguet and Lo Jacono (2014)	1	100	$40/\pi$	0.572
González Cornejo et al. (2017)	1	100	1	0.560
Navrose and Mittal (2017)	1	100	30–150	∼0.55
Zhao et al. (2015)	1	150	2	0.591
Garg et al. (2019)	1	150	2	0.581
Present computations	1	300	10	0.570
Mittal and Singh (2005)	2	33	4.73	0.433
Étienne and Pelletier (2012)	2	30–45	0	0.428–0.567
Prasanth et al. (2011)	2	∼77.15	2	0.583
Prasanth et al. (2011)	2	∼82.9	10	0.559
Prasanth and Mittal (2008)	2	∼86.85	10	0.571
Singh and Mittal (2005)	2	100	10	0.572

In Fig. 16 the oscillation amplitude $\hat{y}_0$ is plotted against the dimensionless damping c^* for damping ratio values between $\zeta = 0.1\%$ and 5%. Note that results belonging to the initial branch and the beginning of the upper branch (where cylinder motion and aerodynamic force coefficients are most likely quasi-periodic signals) are not shown in the figure. It can be seen that, as expected, the peak oscillation amplitude $\hat{y}_{0max}$ decreases with ζ, and occurs at increasing c^*. This figure shows also the $\hat{y}_{0max}$ curve suggested by Konstantinidis (2013), where $k_c = 0.46$ is applied. As seen, this empirical relationship predicts the peak vibration amplitude very well for damping ratio values of $\zeta = 3\%$ and 5%. It is also shown that peak response data from the current CFD computations for $\zeta = 1\%$ and those predicted by Konstantinidis (2013) (using $k_c = 0.46$) compare relatively well. However, peak oscillation amplitude is overpredicted for $\zeta = 0.1\%$ and 0.5%.

Peak cylinder response has been investigated extensively in the literature mainly in the high-*Re* domain. Govardhan and Williamson (2006) and Klamo et al. (2006) found that Reynolds number and the mass-damping parameter $(m^* + C_A)\zeta_A$ have a substantial effect on $\hat{y}_{0max}$. Although Govardhan and Williamson (2006) carried out experiments in the range of $Re = 10^3 - 10^4$, they collected CFD data for low-Reynolds-number flows. Table 6 summarizes peak oscillation amplitude data $\hat{y}_{0max}$ currently available in the literature for undamped low-Reynolds-number vortex-induced vibrations, and $\hat{y}_{0max}$ obtained in this study. In this table the most important parameters (DoF, *Re*, and m^*) are also included. It can be seen that $\hat{y}_{0max}$ is a weak function of the Reynolds number in the range of $Re \cong 70 - 300$; peak vibration amplitude is fairly constant in this range. This finding agrees well with that of Govardhan and Williamson (2006). Surprisingly, comparing transverse-only and two-degree-of-freedom VIV results, there is no significant difference in the peak response data. However, between $Re = 30$ and 70 the peak oscillation amplitude depends highly on *Re* for both 1DoF and 2DoF cases; $\hat{y}_{0max}$ seems to increase with the Reynolds number.

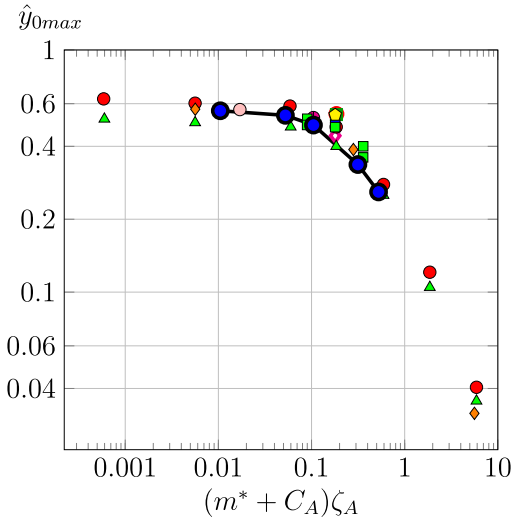

Fig. 17. Peak vibration amplitude values against mass-damping parameter; comparison of currently obtained results (—●—) with those obtained by Anagnostopoulos and Bearman (1992) (●), Nomura (1993) (▲), Anagnostopoulos (1994) (■), Wei et al. (1995) (◆), Newman and Karniadakis (1996) ($m^* = 1$, ●), Newman and Karniadakis (1996) ($m^* = 10$, ▲), Schulz and Kallinderis (1998) (■), Zhou et al. (2004) (◆), Leontini et al. (2006b) (●), Yang et al. (2008) (⬠), Bahmani and Akbari (2010) (■), and Han et al. (2016) (○). (For interpretation of the references to colour in this figure legend, the reader is referred to the web version of this article.)

For non-zero damping ratio cases the Griffin plot is used for comparison, where the peak oscillation amplitude values $\hat{y}_{0max}$ are shown against $(m^* + C_A)\zeta_A$ (Griffin, 1980). Here ζ_A is the damping ratio in which fluid added mass is included. Fig. 17 shows the Griffin plot, where $\hat{y}_{0max}$ obtained in this study and the values available in the literature are compared. The scales are logarithmic on both horizontal and vertical axes. It is very important to emphasize that Reynolds number is not identical in the studies whose results are compiled in Fig. 17; *Re* varies in $Re \leq 300$. Nonetheless, the computed/measured data points collapse almost onto a single curve; only a small scatter is observed. This observation is in contrast with the tendencies in the high-*Re* domain; in those cases $\hat{y}_{0max}$ shows high scatter (Griffin, 1980; Govardhan and Williamson, 2006). Govardhan and Williamson (2006) employed experiments for $\zeta = 0\%$, and showed that the peak oscillation amplitude varies strongly with *Re*. They realized that by normalizing $\hat{y}_{0max}$ obtained for non-zero damping by the peak vibration amplitudes for $\zeta = 0\%$, and plotting it against mass-damping parameter, the high scatter is eliminated. That plot is always referred to as the "modified Griffin plot". However, Govardhan and Williamson (2006) also showed that peak oscillation amplitude is almost constant for low Reynolds numbers. The present findings harmonize with their results (see Table 6). This fact explains why $\hat{y}_{0max}$ data points obtained for different Reynolds numbers collapse very well in the Griffin plot (see Fig. 17).

4.4. Investigation of frequency spectra and vortex formation

In Section 4.1 the harmonic oscillator model is described in detail. Rearranging Eq. (13), the following expression is obtained:

$$\hat{C}_y \sin \Phi = 4\pi^3 \frac{f^* \hat{y}_0}{U^*} m^* \zeta . \tag{22}$$

This expression shows that $\hat{C}_y \sin \Phi$ (responsible for the mechanical energy transfer) varies linearly with $f^* \hat{y}_0 / U^*$, where the proportionality factor is proportional to the mass-damping parameter $m^* \zeta$. Fig. 18 shows $\hat{C}_y \sin \Phi$ against $4\pi^3 f^* \hat{y}_0 / U^*$ for different damping values between $\zeta = 0\%$ and 5% and constant $m^* = 10$. Empty and filled symbols refer to data points belonging to upper and lower branches, respectively. Dashed lines represent the results from the harmonic oscillator model described by Eq. (22) and the numbers (belonging to the dashed lines) show damping ratio values. It can be seen in Fig. 18 that harmonic approximation seems to be accurate in the lower branch and at the beginning of the upper branch. However, at the remaining part of the upper branch the results are far from the harmonic solutions, which suggests that in these domains transverse fluid force is not a harmonic function of time. The results presented earlier are consistent with this proposal. For undamped vibrations we found very high detuning values (around $f^* - f^*_{C_y} = -0.2$) in the *UB*(*V*) subdomain, which may refer to the fact that the most remarkable frequency in the spectra of C_y is equal to the double of the vibration frequency. Besides, in *UB*(*III*) and *UB*(*IV*) the time-dependent transverse phase shows unreasonable fluctuations, which may also indicate the occurrence of higher order harmonics in the spectra of the transverse fluid force. In order to confirm the non-harmonic nature of C_y (in some ranges), time histories and frequency spectra of cylinder

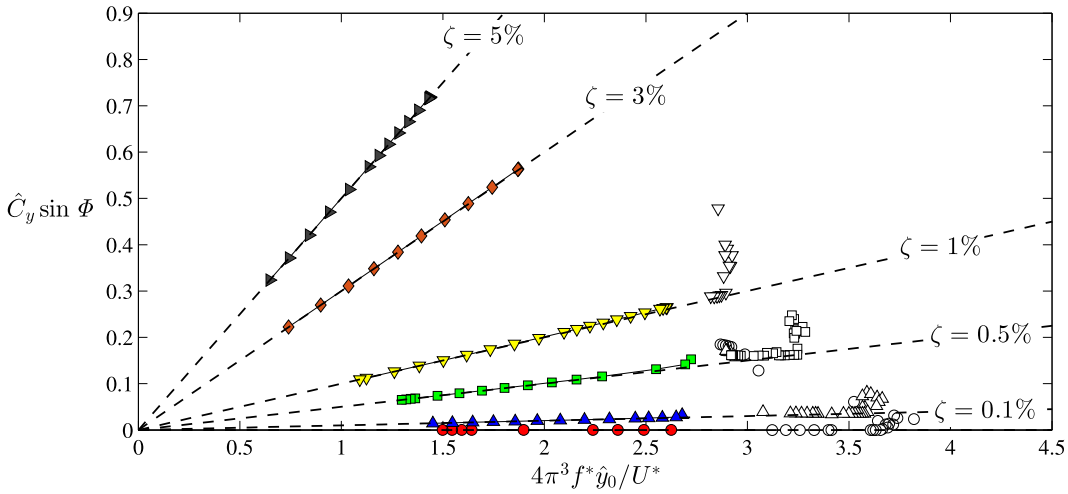

Fig. 18. $\hat{C}_y \sin \Phi$ against $4\pi^3 f^* \hat{y}_0 / U^*$ in the upper branch (empty symbols) and in the lower branch (filled symbols) for $\zeta = 0\%$ (—●—), 0.1% (—▲—), 0.5% (—■—), 1% (—▼—), 3% (—◆—), and 5% (—▶—). The dashed lines represent solutions obtained from the harmonic oscillator model given by Eq. (22). (For interpretation of the references to colour in this figure legend, the reader is referred to the web version of this article.)

displacement and transverse fluid force coefficient are further analyzed. The analyses are carried out first for undamped cylinder vibrations and then for non-zero damping ratio values.

4.4.1. Undamped cylinder vibrations

Fig. 19 shows the time histories of non-dimensional cylinder displacement (left-hand side of the figure) and transverse fluid force (middle) at different U^* values in the initial (see Fig. 19a), upper (Fig. 19b–e), and lower branches (Fig. 19f) for $\zeta = 0\%$. Frequency spectra of signals (displacement and transverse fluid force) normalized by the cylinder's natural frequency in vacuum obtained using Fast Fourier Transform (FFT) are shown in the right-hand plots of the figures. Here *PSD* denotes *Power Spectral Density*, and the vertical axis has logarithmic scale.

It can be seen in Fig. 19a that the signals in the initial branch show a quasi-periodic nature; y_0 and C_y contain multiple frequency components. This is the reason why time-dependent transverse phase shows random fluctuations in the same reduced velocity range (see Fig. 5c). At $U^* = 4$ high jumps are observed in $y_{0'}$ and f/f_N at the location where the cylinder response shifts from the initial to the upper branch (see Fig. 3). The high cylinder displacement in the upper branch can be observed in Fig. 19b. This figure shows also that in the *UB*(*I*) subregion ($4 < U^* \leq 4.28$, see the classification in Table 4) the cylinder motion and the transverse fluid force are quasi-periodic signals. These effects are expected, because in this range the time-dependent transverse phase shows random variation (see Fig. 7a). Due to the quasi-periodic behavior, the frequency spectra of y_0 and C_y contain multiple frequency components, of which $f/f_N \cong 1$ and 3 have the highest *PSD* values. Note that $f/f_N \cong i$ frequency peak is usually referred to as the ith harmonic frequency component. Switching to *UB*(*II*) (which occurs in $4.28 < U^* \leq 4.35$, see Table 4), the time-varying phase differences show periodic variations (see Fig. 9a), which suggests periodic cylinder vibrations. It can be seen in Fig. 19c that, reassuringly, both y_0 and C_y are periodic signals; transverse fluid force contains relevant frequency components at $f/f_N \cong 1$ (highest intensity) and 3 (relatively low intensity), while in the spectrum of cylinder displacement only $f/f_N \cong 1$ is identified (Fig. 19c).

Increasing the reduced velocity through *UB*(*III*) (between $U^* = 4.36$ and 4.48), slightly above the jumps found in $C_{y'}$ and $C_{v'}$ (see Fig. 4), the transverse fluid force and the cylinder displacement become quasi-periodic again (Fig. 19d). These signals show similar behavior to the time-varying phases; in *UB*(*III*) random oscillations have been found in Φ and Φ_v. Besides, in the frequency spectra of C_y first, second and third harmonic components are identified as high-intensity peaks. Varying reduced velocity in the remaining part of the upper branch (in *UB*(*IV*) and *UB*(*V*), see Table 4), C_y is found to be periodic again, and the $f/f_N \cong 2$ frequency component is found to play a significant role in its spectra (see Fig. 19e). This finding, which we expected, explains why the computational results do not agree with the harmonic solutions represented by Eq. (22) at some parts of the upper branch (see Fig. 18), and implies why the transverse phase shows unreasonably high fluctuations in *UB*(*III*) (Fig. 9c).

Many studies have dealt with the frequency components occurring in the spectra of transverse fluid force. Without aiming to give an exhaustive list, Jauvtis and Williamson (2004), Dahl et al. (2006, 2007, 2010), and Wang et al. (2017) discussed the relevance of first and third harmonic components in C_y for two-degree-of-freedom vortex-induced vibrations. However, the second harmonic component is not so typical in VIV. Bao et al. (2012) and Dorogi and Baranyi (2019) investigated also two-degree-of-freedom VIV, and they identified the $f/f_N = 2$ frequency peak in the spectra of C_y. Dorogi and Baranyi (2019) showed that the second harmonic frequency component has a fundamental effect on the path of the cylinder; it makes the cylinder path asymmetric.

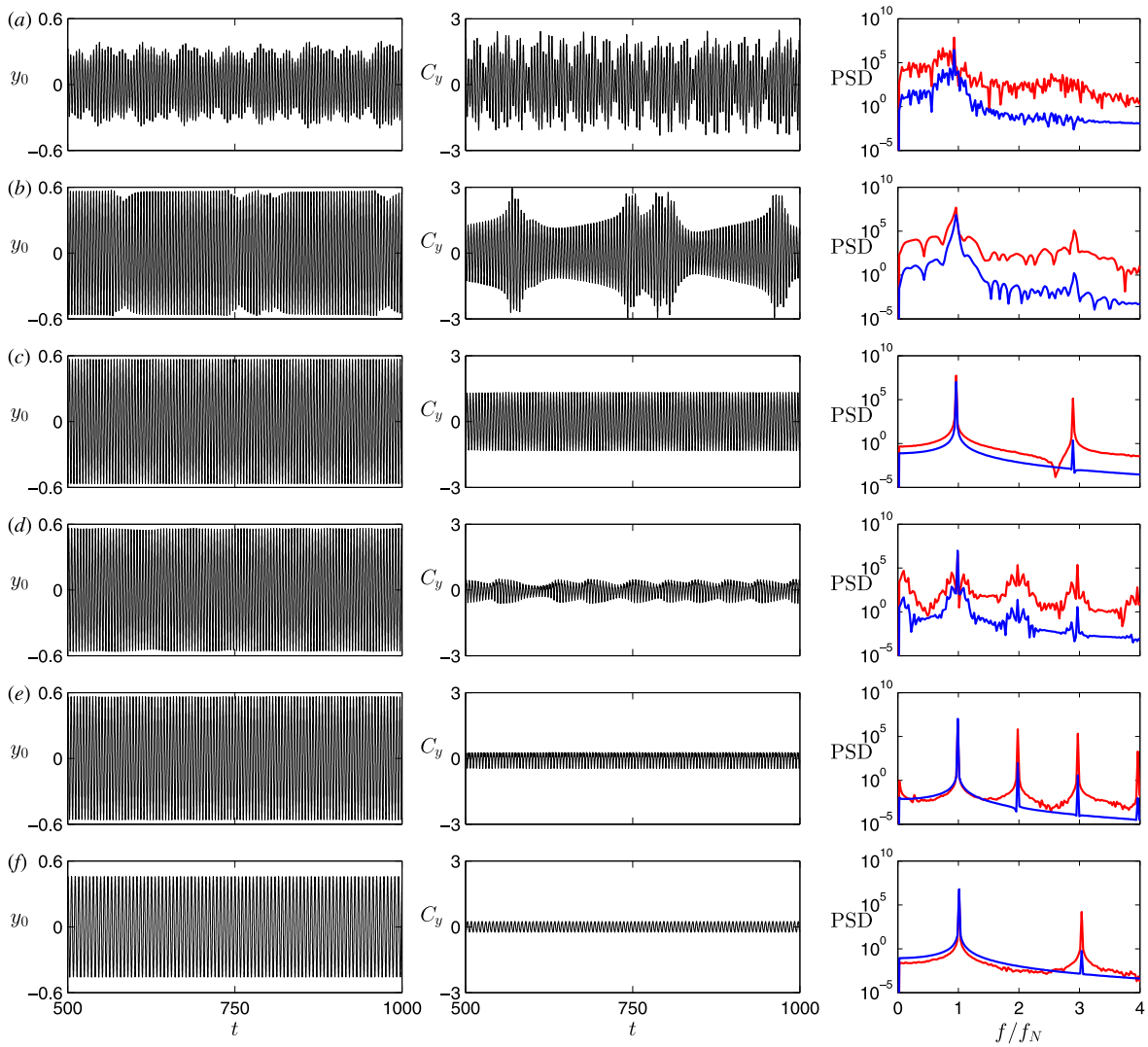

Fig. 19. Time histories (left and middle) and fast Fourier spectra (right) of cylinder displacement and transverse fluid force at $U^* = 4$ (a): initial branch, 4.2 (b): $UB(I)$, 4.3 (c): $UB(II)$, 4.4 (d): $UB(III)$, 4.6 (e): $UB(IV)$, and 5.5 (f): lower branch for $\zeta = 0\%$. In the FFT spectra red and blue colors mark the frequency spectra of transverse fluid force and cylinder displacement, respectively. (For interpretation of the references to colour in this figure legend, the reader is referred to the web version of this article.)

In the lower branch (from $U^* = 4.9$ to 5.9) both y_0 and C_y are periodic signals. As seen in Fig. 19f, the second harmonic component completely disappears, only $f/f_N = 1$ and 3 peaks remain (see Fig. 19f). Since the intensity of $f/f_N = 3$ is much smaller than the first harmonic component, the $f/f_N = 3$ peak influences the vibration only slightly. This is why data points corresponding to the lower branch fit very well on the model results based on harmonic approximations (see Fig. 18).

As can be seen in Fig. 6, a high detuning value of $f^* - f^*_{C_y} \cong -0.2$ occurs at the end of the upper branch (in $UB(V)$, see Table 4), which value approximately agrees with the Strouhal number at $Re = 300$. Since the vibration frequency in this range is also close to the Strouhal number, this detuning value can only be reached when the second harmonic frequency component is the most dominant in the spectra of C_y. Although we showed that $f/f_N \cong 2$ occurs in the upper branch, it was not confirmed whether it is the most relevant harmonic in the $UB(V)$ subdomain. Fig. 20 shows the frequency spectra of transverse fluid force at different U^* values, where Power Spectral Density normalized by the maximum PSD in the spectra $PSD_{norm} = PSD/PSD_{max}$ is plotted against f/f_N. Note that vertical axis is scaled linearly. It can be seen that in $UB(IV)$ (see Fig. 20a) $f/f_N \cong 1$ is the most intensive peak, while the normalized PSD at $f/f_N \cong 2$ is very low. As expected, in $UB(V)$ the roles of first and second harmonic components are switched; $f/f_N \cong 2$ is the most dominant, while the normalized PSD of $f/f_N \cong 1$ is relatively low (see Fig. 20b and c). However, switching to the lower branch causes a dramatic change in

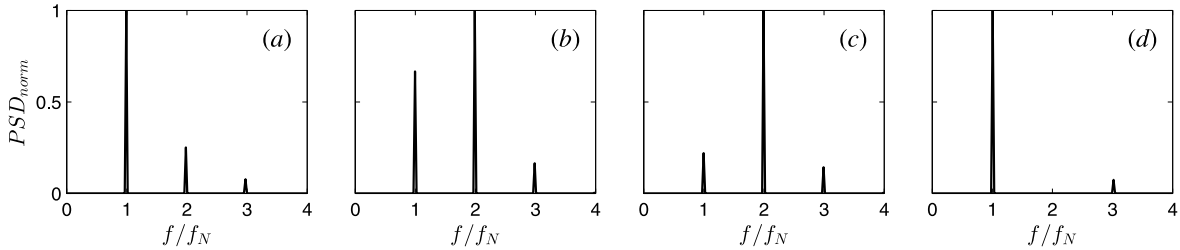

Fig. 20. Frequency spectra of transverse fluid force at $U^* = 4.5$ (a): $UB(IV)$, 4.8 (b): $UB(V)$, 4.89 (c): $UB(V)$, and 4.9 (d): lower branch for $\zeta = 0\%$.

the FFT of C_y. As shown in Fig. 20d, the second harmonic component completely disappears but first and third harmonic components remain in the spectra, where $f/f_N \cong 1$ is the most relevant component.

Singh and Mittal (2005), Prasanth and Mittal (2008), and Bahmani and Akbari (2010) found that the formation of vortices shedding from the body is sensitive to the value of reduced velocity. Fig. 21 shows the vortex structures at the same U^* values where the time histories and FFT spectra of cylinder displacement and transverse fluid force were previously analyzed (see Fig. 19). As shown in Fig. 19a, y_0 and C_y are quasi-periodic signals in the initial branch, that is, the vortex structures at the corresponding reduced velocity values change dynamically with time (see Fig. 21a).

Shifting to the $UB(I)$ subdomain the cylinder motion and the fluid force coefficients are still quasi-periodic signals, that is, the vortex structure is also highly time-dependent (see Fig. 21b). It was found that time histories of y_0 and C_y are periodic in $UB(II)$, and the FFT spectra of C_y contain relevant frequency peaks at $f/f_N = 1$ and 3 (Fig. 19c). It can be seen in Fig. 21c that in the corresponding range a $2P_0$ wake mode seems to develop, which means that two pairs of vortices are shed from the cylinder in each motion period, but the secondary vortex in each pair is much weaker than the primary vortex (Morse and Williamson, 2009). Morse and Williamson (2009) found that when the vortex pair is moving downstream from the cylinder, the secondary vortex decays, which is also seen in Fig. 21c. Khalak and Williamson (1997, 1999) identified $2P$ vortex shedding mode in the upper branch, where strengths of the primary and secondary vortex are approximately identical. It has to be noted that the $2P_0$ vortex structure has not been found earlier for low-Reynolds-number cases.

At the closing part of the upper branch [i.e. in $UB(III)$, $UB(IV)$ and $UB(V)$] the $f/f_N \cong 2$ peak was found to occur, which strongly influences the vortex structure (Bao et al., 2012; Dorogi and Baranyi, 2019). Although the structure of vortices changes in $UB(III)$, due to the modulations in the aerodynamic forces, the wake modes are similar to the $P+S$ vortex shedding mode (Fig. 21d). Here $P+S$ denotes that a pair of vortices and a single vortex are shed from the cylinder. In the $UB(IV)$ and $UB(V)$ subranges time traces of y_0 and C_y return back to periodic. As seen in Fig. 20, the second harmonic frequency component plays an important role in C_y in these subdomains, which makes the vortex structure asymmetric; stable $P+S$ modes are seem to form here (see Fig. 21e). However, the vorticity contours shown in Fig. 21e are not a regular $P+S$ mode. As can be seen, the positive vortex (in red) in the vortex pair is noticeably smaller than the negative vortex (blue). In the $P+S$ wake mode obtained by Blackburn and Henderson (1999) using forced vibration computations, the size of the positive and negative vortex are approximately equal. Besides, it can be seen that in the top row vortex train, a small positive vortex is connected to every second negative vortex. This suggests that a $P+S$ vortex structure is shed in every two oscillation cycles. In order to investigate the dynamics of vortex shedding, further analyses are planned, but these are not in the scope of this paper.

As shown in Figs. 19 and 20, in the lower branch the $f/f_N = 2$ frequency peak completely disappears from the spectra of C_y. For this reason the vortex structure becomes symmetric; $2S$ wake modes (two single vortices) are found in this domain ($4.89 < U^* \leq 5.9$, see Fig. 21f).

4.4.2. Damped cylinder vibrations

It was shown earlier that structural damping ratio strongly influences the cylinder response; a three-branch response was identified for $\zeta \leq 1\%$, and two-branch response for $\zeta = 3\%$ and 5%. It can be seen in Fig. 13c that for $\zeta = 0.5\%$, at the boundary separating upper and lower branches no unbounded change can be observed in the transverse phase, which is in contrast with the findings for $\zeta = 0\%$. It was confirmed in Section 4.4.1 that the unbounded increase of transverse phase (which is closely related to the high detuning value of $f^* - f^*_{C_y}$) is caused by the fact that second harmonic frequency component is the most dominant in the spectrum of C_y. For this reason, the lack of unbounded variation in Φ for $\zeta = 0.5\%$ suggests that the intensity of $f/f_N \cong 2$ is not the highest in the upper↔lower branch transition range. Fig. 22 shows PSD_{norm} against f/f_N at different reduced velocity values in the upper branch for $\zeta = 0.5\%$. This figure corroborates the former assumption; the role of $f/f_N \cong 2$ increases with U^* but at the boundary of the upper and lower branches (at $U^* = 4.688$, see Fig. 22d) the first harmonic component dominates, and $f/f_N \cong 2$ occurs only with low intensity. The additional findings related for example to the vortex formation downstream from the cylinder hold true for the $\zeta \leq 1\%$ range where three-branch responses are found; these are not repeated here again.

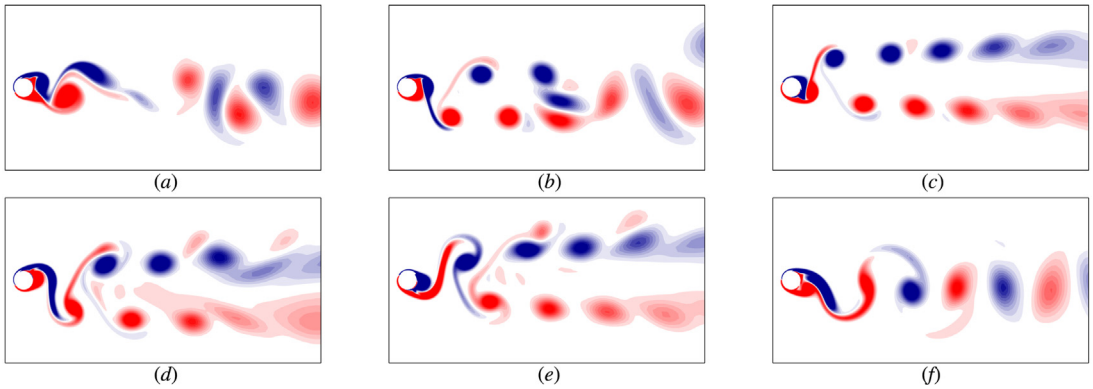

Fig. 21. Vortex structures (red: positive vorticity, blue: negative) at $U^* = 4$ (a): initial branch, 4.2 (b): $UB(I)$, 4.3 (c): $UB(II)$, 4.4 (d): $UB(III)$, 4.6 (e): $UB(IV)$, and 5.5 (f): lower branch for $\zeta = 0\%$. (For interpretation of the references to colour in this figure legend, the reader is referred to the web version of this article.)

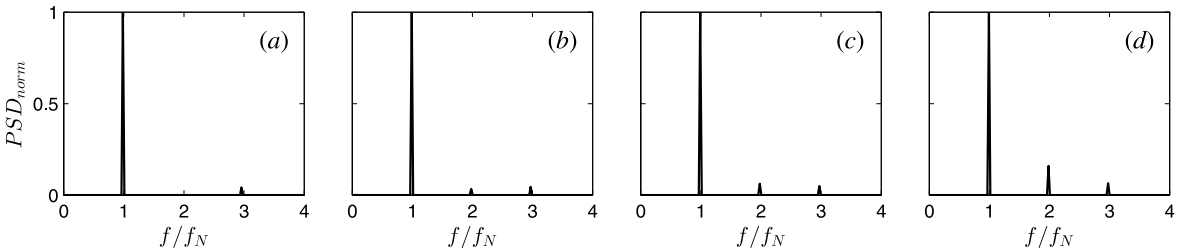

Fig. 22. Frequency spectra of transverse fluid force at $U^* = 4.5$ (a), 4.56 (b), 4.6 (c), and 4.688 (d) for $\zeta = 0.5\%$.

As mentioned above, increasing the structural damping ratio over $\zeta = 1\%$, only initial and lower branches are found, the upper branch disappears from the response. The question arises what the difference is between three- and two-branch responses in terms of frequency spectra and vortex structures. Fig. 23 shows the frequency spectra of cylinder displacement and transverse fluid force (top row), and vortex contours (bottom row) at different reduced velocity values for $\zeta = 3\%$. As can be seen in Fig. 23a, the FFT spectra of transverse fluid force for $U^* = 4.2$ contains several frequency components, that is, y_0 and C_y are quasi-periodic signals, and vortex structures are highly time-dependent but similar to the regular $2S$ vortex shedding mode. The above-mentioned properties of flow and vibration characteristics between reduced velocity values of $U^* = 4$ and 4.66 are similar to those of the initial branch at the $\zeta \leq 1\%$ domain. Increasing reduced velocity up to $U^* = 4.68$, cylinder response reaches the lower branch, where both y_0 and C_y return back to periodic. In contrast to the results reported in the low-damping domain, vibration frequency does not lock exactly to the cylinder's natural frequency in vacuum (see also Fig. 12). Fig. 23b and c show the spectra of y_0 and C_y in the range where oscillation amplitude is relatively high. As seen, first and third harmonic frequency components can be found in the spectra of C_y. Since the peak of $f/f_N = 2$ is not present in the spectra, $2S$ vortex structures are captured in these computational points.

5. Conclusions

In this study two-dimensional incompressible Newtonian fluid flow around a circular cylinder undergoing transverse-only vortex-induced vibrations is investigated at fixed Reynolds number and mass ratio values of $Re = 300$ and $m^* = 10$, respectively. Reduced velocity based on the natural frequency of the cylinder in vacuum is varied between $U^* = 2.5$ and 7.5, and the structural damping ratio is chosen to be in the range of $\zeta = 0 - 5\%$.

5.1. Undamped ($\zeta = 0\%$) vibrations

Plotting the root-mean-square (rms) values of cylinder displacement $y_{0'}$ and the vibration frequency normalized by the cylinder's natural frequency in vacuum f/f_N against reduced velocity, a three-branch cylinder response can be observed, which has up to now not been identified for low Reynolds numbers. Time-averaged phase differences of transverse fluid force and vortex force $\overline{\Phi}$ and $\overline{\Phi}_v$ relative to the cylinder displacement (referred to as transverse and vortex phases, respectively) are used to confirm the existence of the upper branch. These time-mean values are computed by time-averaging the time-dependent phase differences (Φ and Φ_v) wrapped in $[-\pi/2; 3\pi/2]$.

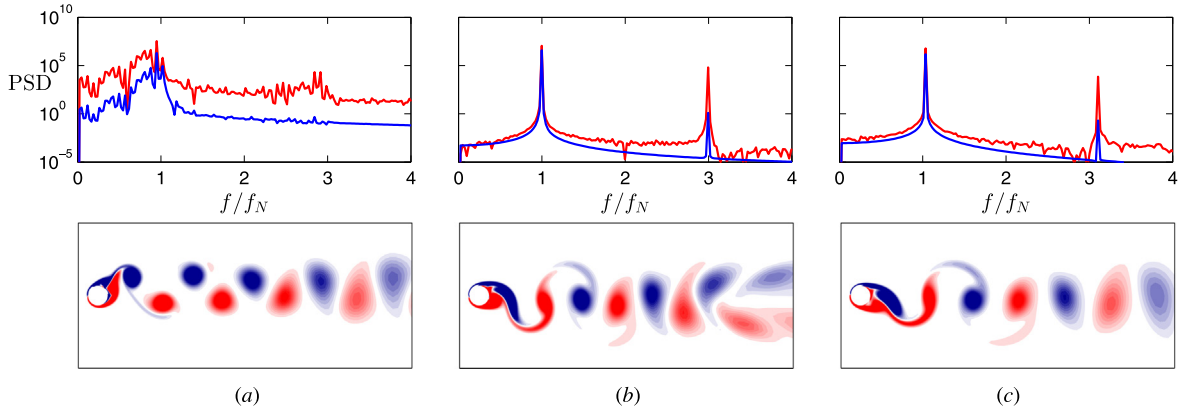

Fig. 23. Frequency spectra of cylinder displacement (blue curves) and transverse fluid force (red curves), and the corresponding vorticity contours (red: positive vorticity, blue: negative) at $U^* = 4.2$ (a), 4.68 (b) and 5.4 (c) for $\zeta = 3\%$. (For interpretation of the references to colour in this figure legend, the reader is referred to the web version of this article.)

The initial branch is found to occur in the range of $3.45 < U^* \leq 4$, where $y_{0'}$ shows rapid increase, and the vibration frequency is relatively far from the natural frequency of the cylinder. In this domain Φ varies around zero, and Φ_v shows an unbounded decrease. Following Pikovsky et al. (2001), the unbounded decrease can be explained by the high positive detuning values $f^* - f^*_{C_v}$, where f^* and $f^*_{C_v}$ are the frequencies of cylinder vibration and vortex force coefficient, respectively.

In the upper branch ($4 < U^* \leq 4.89$) relatively high oscillation amplitudes are observed, and the vibration frequency is slightly below the cylinder's natural frequency. Based on the tendencies observed in the time-dependent phases, the upper branch can be divided into five subdomains. In $UB(I)$ (between $U^* = 4$ and 4.28), $f^* - f^*_{C_v} < 0$, that is, vortex phase increases. Since the detuning is very small compared to that observed in the initial branch, the unbounded variation in Φ_v is replaced by epochs and phase slips. At the time interval of an epoch, wrapped vortex phase varies around π (180°) (satisfying an important condition of the upper branch), and at phase slips Φ_v deviates significantly from π. Since epochs lengthen with U^*, $\overline{\Phi}_v$ approaches 180° when U^* is increased. Besides, time-averaged transverse phase $\overline{\Phi}$ is approximately zero in this range.

At the rest of the upper branch (i.e. from $UB(II)$ to $UB(V)$), although the corresponding phases show both periodic and random features, they vary around $\overline{\Phi} = 0°$ and $\overline{\Phi}_v = 180°$, which are the conditions that characterize the upper branch. In $UB(III)$ and $UB(IV)$ ($4.35 < U^* \leq 4.7$) second harmonic frequency component $f/f_N \cong 2$ is identified as a dominant peak in the spectra of transverse fluid force, which causes the unreasonably high fluctuations in the transverse phase. However, in $UB(V)$ (between $U^* = 4.7$ and 4.89) $f/f_N \cong 2$ is found to be the most dominant frequency component, which explains the high detuning values around $f^* - f^*_{C_y} = -0.2$, and the unbounded increase in transverse phase. Here $f^*_{C_y}$ is the frequency of the transverse fluid force coefficient.

The lower branch is located in $4.89 < U^* \leq 5.9$ (above a sudden jump in the cylinder response), where $y_{0'}$ is in the intermediate range, and f is slightly above f_N. The results obtained in the lower branch agree with those expected, $\overline{\Phi} \cong \overline{\Phi}_v \cong 180°$. The fluctuations observed in the time-dependent phases decrease with U^*.

Different vorticity contours are identified in this study. In the initial and lower branches the classic $2S$ wake mode is found, while in the upper branch $2P_O$ and $P+S$ modes seem to occur. It was found that the occurrence of the asymmetrical vortex structure is closely related to the second harmonic frequency component identified in the spectra of transverse fluid force. This finding agrees with those reported in the literature (Bao et al., 2012; Dorogi and Baranyi, 2019).

5.2. Damped vibrations

Similar to the experimental findings for high Reynolds numbers, increasing structural damping ratio leads to the transition from a three-branch to a two-branch response. In $\zeta \leq 1\%$ the upper branch is found to occur, whose reduced velocity range decreases with damping ratio. For $\zeta = 3\%$ and 5%, the upper branch completely disappears from the response, only initial and lower branches remain.

The three-branch response for damped vibrations shows similar characteristics to that for $\zeta = 0\%$. In the initial branch time history of vortex phase shows unbounded decreases. Switching to the upper branch, although Φ_v contains epochs and phase slips, it does not show increasing effects. The reduced velocity range where Φ increases unboundedly (close to the boundary separating upper and lower branches) diminishes with the damping ratio; at $\zeta \geq 0.5\%$ this domain is not identified, Φ is approximately constant at the higher boundary of the upper branch. For $\zeta = 0.5\%$ the $f/f_N \cong 2$ peak does not play a dominant role in the spectra of transverse fluid force (its intensity is low), which explains why Φ is approximately constant at the higher end of the upper branch.

Mechanical energy transfer is approximately zero for undamped cylinder vibrations, because time-averaged transverse and vortex phases are approximately 0° or 180°. Small discrepancies occur in the initial branch and in the transition ranges which bound the upper branch. As the damping ratio is increased, the mechanical energy transfer shifts upwards, because $\overline{\Phi}$ and $\overline{\Phi}_v$ are allowed to be between 0° and 180°.

The peak oscillation amplitudes $\hat{y}_{0max}$ for $\zeta = 3\%$ and 5% compares very well with the empirical relationship of $\hat{y}_{0max} = 0.46/c^*$ suggested by Konstantinidis (2013). Although $\hat{y}_{0max}$ for $\zeta = 1\%$ shows relatively good agreement, peak response data for $\zeta = 0.1\%$ and 0.5% are far from the empirical curve. Peak response data obtained in this study and those available in the literature plotted against mass-damping parameter (i.e. using the "Griffin plot") collapse almost into a single curve. This finding is in contrast to the experimental results at high Reynolds numbers; large scatter is observed in those cases. The possible reason for the small scatter is that peak vibration amplitude is roughly independent of Reynolds number in the low-*Re* domain.

CRediT authorship contribution statement

Dániel Dorogi: Conceptualization, Software, Validation, Formal analysis, Writing - original draft, Writing - review & editing, Visualization. **László Baranyi:** Software, Writing - review & editing, Supervision.

Declaration of competing interest

The authors declare that they have no known competing financial interests or personal relationships that could have appeared to influence the work reported in this paper.

Acknowledgment

We would like to express our sincere thanks to Dr. Efstathios Konstantinidis (University of Western Macedonia, Kozani, Greece) for discussions about different aspects of vortex-induced vibrations which helped us to construct this manuscript.

We would like to thank the anonymous reviewers for their careful revision of the manuscript and their many insightful comments and suggestions.

This research was supported by the European Union and the Hungarian State, co-financed by the European Regional Development Fund in the framework of the GINOP-2.3.4-15-2016-00004 project, aimed to promote the cooperation between the higher education and the industry.

References

Anagnostopoulos, P., 1994. Numerical investigation of response and wake characteristics of a vortex-excited cylinder in a uniform stream. J. Fluids Struct. 8, 367–390. http://dx.doi.org/10.1006/jfls.1994.1018.

Anagnostopoulos, P., Bearman, P., 1992. Response characteristics of a vortex-excited cylinder at low Reynolds numbers. J. Fluids Struct. 6, 39–50. http://dx.doi.org/10.1016/0889-9746(92)90054-7.

Bahmani, M., Akbari, H., 2010. Effects of mass and damping ratios on VIV of a circular cylinder. Ocean Eng. 37, 511–519. http://dx.doi.org/10.1016/j.oceaneng.2010.01.004.

Bao, Y., Huang, C., Zhou, D., Tu, J., Han, Z., 2012. Two-degree-of-freedom flow-induced vibrations on isolated and tandem cylinders with varying natural frequency ratios. J. Fluids Struct. 35, 50–75. http://dx.doi.org/10.1016/j.jfluidstructs.2012.08.002.

Baranyi, L., 2008. Numerical simulation of flow around an orbiting cylinder at different ellipticity values. J. Fluids Struct. 24 (6), 883–906. http://dx.doi.org/10.1016/j.jfluidstructs.2007.12.006.

Barkley, D., Henderson, R., 1996. Three dimensional Floquet stability analysis of the wake of a circular cylinder. J. Fluid Mech. 322, 215–241. http://dx.doi.org/10.1017/S0022112096002777.

Bearman, P., 1984. Vortex shedding from oscillating bluff bodies. Annu. Rev. Fluid Mech. 16, 195–222. http://dx.doi.org/10.1146/annurev.fl.16.010184.001211.

Bearman, P., 2011. Circular cylinder wakes and vortex-induced vibrations. J. Fluids Struct. 27 (5–6), 648–658. http://dx.doi.org/10.1016/j.jfluidstructs.2011.03.021.

Bearman, P., Obasaju, E., 1982. An experimental study of pressure fluctuations fixed and oscillating square-section cylinders. J. Fluid Mech. 119, 297–321. http://dx.doi.org/10.1017/S0022112082001360.

Bernitsas, M., Raghavan, K., Ben-Simon, Y., Garcia, E., 2008. VIVACE (Vortex Induced Vibration Aquatic Clean Energy): a new concept in generation of clean and renewable energy from fluid flow. J. Offshore Mech. Arct. Eng. 130 (4), 041101. http://dx.doi.org/10.1115/1.2957913, (15 pages).

Blackburn, H., Henderson, R., 1996. Lock-in behavior in simulated vortex-induced vibration. Exp. Therm Fluid Sci. 12 (2), 184–189. http://dx.doi.org/10.1016/0894-1777(95)00093-3.

Blackburn, H., Henderson, R., 1999. A study of two-dimensional flow past an oscillating cylinder. J. Fluid Mech. 385, 255–286. http://dx.doi.org/10.1017/S0022112099004309.

Blevins, R., 1990. Flow-Induced Vibration. Van Nostrand Reinhold Co., Inc., New York.

Bourguet, R., Lo Jacono, D., 2014. Flow-induced vibrations of a rotating cylinder. J. Fluid Mech. 740, 342–380. http://dx.doi.org/10.1017/jfm.2013.665.

Brika, D., Laneville, A., 1993. Vortex-induced vibration of a long flexible circular cylinder. J. Fluid Mech. 250, 481–508. http://dx.doi.org/10.1017/S0022112093001533.

Dahl, J., Hover, F., Triantafyllou, M., 2006. Two-degree-of-freedom vortex-induced vibrations using a force assisted apparatus. J. Fluids Struct. 22 (6–7), 807–818. http://dx.doi.org/10.1016/j.jfluidstructs.2006.04.019.

Dahl, J., Hover, F., Triantafyllou, M., Dong, S., Karniadakis, G., 2007. Resonant vibrations of bluff bodies cause multivortex shedding and high frequency forces. Phys. Rev. Lett. 99, 144503. http://dx.doi.org/10.1103/PhysRevLett.99.144503, (4 pages).

Dahl, J.M., Hover, F.S., Triantafyllou, M.S., Oakley, O.H., 2010. Dual resonance in vortex-induced vibrations at subcritical and supercritical Reynolds numbers. J. Fluid Mech. 643, 395–424. http://dx.doi.org/10.1017/S0022112009992060.

Dorogi, D., Baranyi, L., 2018. Numerical simulation of a freely vibrating circular cylinder with different natural frequencies. Ocean Eng. 158, 196–207. http://dx.doi.org/10.1016/j.oceaneng.2018.03.079.

Dorogi, D., Baranyi, L., 2019. Occurrence of orbital cylinder motion for flow around freely vibrating circular cylinder in uniform stream. J. Fluids Struct. 87, 228–246. http://dx.doi.org/10.1016/j.jfluidstructs.2019.03.004.

Étienne, S., Pelletier, D., 2012. The low Reynolds number limit of vortex-induced vibrations. J. Fluids Struct. 31, 18–29. http://dx.doi.org/10.1016/j.jfluidstructs.2012.02.006.

Evangelinos, C., Karniadakis, G.E., 1999. Dynamics and flow structures in the turbulent wake of rigid and flexible cylinders subject to vortex-induced vibrations. J. Fluid Mech. 400, 91–124. http://dx.doi.org/10.1017/S0022112099006606.

Feng, C., 1968. The Measurement of Vortex Induced Effects in Flow Past Stationary and Oscillating Circular and D-Section Cylinders (Master's thesis). University of British Columbia, http://dx.doi.org/10.14288/1.0104049, URL: https://open.library.ubc.ca/collections/ubctheses/831/items/1.0104049.

Garg, H., Soti, A., Bhardwaj, R., 2019. Vortex-induced vibration of a cooled circular cylinder. Phys. Fluids 31, 083608. http://dx.doi.org/10.1063/1.5112140, (17 pages).

González Cornejo, F., Cruchaga, M., Celentano, D., 2017. Modelling low Reynolds number vortex-induced vibration problems with a fixed mesh fluid-solid interaction formulation. Phys. Fluids 29, 113601. http://dx.doi.org/10.1063/1.4996868, (9 pages).

Govardhan, R., Williamson, C., 2000. Modes of vortex formation and frequency response for a freely-vibrating cylinder. J. Fluid Mech. 420, 85–110. http://dx.doi.org/10.1017/S0022112000001233.

Govardhan, R., Williamson, C., 2006. Defining the 'modified Griffin plot' in vortex-induced vibration: revealing the effect of Reynolds number using controlled damping. J. Fluid Mech. 561, 147–180. http://dx.doi.org/10.1017/S0022112006000310.

Griffin, O., 1980. Vortex-excited cross-flow vibrations of a single cylindrical tube. ASME J. Press. Vessel Technol. 102, 158–166. http://dx.doi.org/10.1115/1.3263315.

Han, X., Lin, W., Zhang, X., Tang, Y., Zhao, C., 2016. Two degree of freedom flow-induced vibration of cylindrical structures in marine environments: frequency ratio effects. J. Mar. Sci. Technol. 21, 479–492. http://dx.doi.org/10.1007/s00773-016-0370-5.

Harlow, F., Welch, J., 1965. Numerical calculation of time-dependent viscous incompressible flow of fluid with free surface. Phys. Fluids 8 (12), 2182–2189. http://dx.doi.org/10.1063/1.1761178.

Jauvtis, N., Williamson, C.H.K., 2004. The effect of two degrees of freedom on vortex-induced vibration at low mass and damping. J. Fluid Mech. 509, 23—62. http://dx.doi.org/10.1017/S0022112004008778.

Kawamura, T., Takami, H., Kuwahara, K., 1986. Computation of high Reynolds number flow around a circular cylinder with surface roughness. Fluid Dyn. Res. 1 (2), 145–162. http://dx.doi.org/10.1016/0169-5983(86)90014-6.

Khalak, A., Williamson, C., 1997. Fluid forces and dynamics of a hydroelastic structure with very low mass and damping. J. Fluids Struct. 11, 973–982. http://dx.doi.org/10.1006/jfls.1997.0110.

Khalak, A., Williamson, C., 1999. Motions, forces and mode transitions in vortex-induced vibrations at low mass-damping. J. Fluids Struct. 13 (7–8), 813–851. http://dx.doi.org/10.1006/jfls.1999.0236.

Klamo, J., Leonard, A., Roshko, A., 2006. The effect of damping on the amplitude and frequency response of a freely vibrating cylinder in cross-flow. J. Fluids Struct. 22 (6–7), 845–856. http://dx.doi.org/10.1016/j.jfluidstructs.2006.04.009.

Koide, M., Tomida, S., Takahashi, T., Baranyi, L., Shirakashi, M., 2002. Influence of cross-sectional configuration on the synchronization of Kármán vortex shedding with the cylinder oscillation. JSME Int. J. Ser. B 45 (2), 249–258. http://dx.doi.org/10.1299/jsmeb.45.249.

Konstantinidis, E., 2013. Apparent and effective drag for circular cylinders oscillating transverse to a free stream. J. Fluids Struct. 39, 418–426. http://dx.doi.org/10.1016/j.jfluidstructs.2013.03.001.

Konstantinidis, E., Zhao, J., Leontini, J., Lo Jacono, D., Sheridan, J., 2019. Excitation and damping fluid forces on a cylinder undergoing vortex-induced vibration. Front. Phys. 7, 185. http://dx.doi.org/10.3389/fphy.2019.00185, (10pages).

Konstantinidis, E., Zhao, J., Leontini, J., Lo Jacono, D., Sheridan, J., 2020. Phase dynamics of effective drag and lift components in vortex-induced vibration at low mass–damping. J. Fluids Struct. 96, 103028. http://dx.doi.org/10.1016/j.jfluidstructs.2020.103028.

Lee, J.H., Bernitsas, M.M., 2011. High-damping, high-Reynolds VIV tests for energy harnessing using the VIVACE converter. Ocean Eng. 38 (16), 1697–1712. http://dx.doi.org/10.1016/j.oceaneng.2011.06.007.

Leontini, J., Stewart, B., Thompson, M., Hourigan, K., 2006a. Wake state and energy transitions of an oscillating cylinder at low Reynolds number. Phys. Fluids 18, 067101. http://dx.doi.org/10.1063/1.2204632, (9 pages).

Leontini, J., Thompson, M., Hourigan, K., 2006b. The beginning of branching behavior of vortex-induced vibration during two-dimensional flow. J. Fluids Struct. 22 (6–7), 857–864. http://dx.doi.org/10.1016/j.jfluidstructs.2006.04.003.

Lighthill, J., 1986. Fundamentals concerning wave loading on offshore structures. J. Fluid Mech. 173, 667–681. http://dx.doi.org/10.1017/S0022112086001313.

Meneghini, J., Bearman, P., 1995. Numerical simulation of high amplitude oscillatory flow about a circular cylinder. J. Fluids Struct. 9, 435–455. http://dx.doi.org/10.1006/jfls.1995.1025.

Mittal, S., Singh, S., 2005. Vortex-induced vibrations at subcritical Re. J. Fluid Mech. 534, 185–194. http://dx.doi.org/10.1017/S0022112005004635.

Morse, T., Williamson, C., 2009. Prediction of vortex-induced vibration response by employing controlled motion. J. Fluid Mech. 634, 5–39. http://dx.doi.org/10.1017/S0022112009990516.

Navrose, Mittal, S., 2017. A new regime of multiple states in free vibration of a cylinder at low Re. J. Fluids Struct. 68, 310–321. http://dx.doi.org/10.1016/j.jfluidstructs.2016.11.003.

Newman, D., Karniadakis, G., 1996. Simulation of flow over a flexible cable: a comparison of forced and flow-induced vibrations. J. Fluids Struct. 10, 439–453. http://dx.doi.org/10.1006/jfls.1996.0030.

Nomura, T., 1993. Finite element analysis of vortex-induced vibrations of bluff cylinders. J. Wind Eng. Ind. Aerodyn. 46–47, 587–594. http://dx.doi.org/10.1016/0167-6105(93)90326-J.

Norberg, C., 2003. Fluctuating lift on a circular cylinder: review and new measurements. J. Fluids Struct. 17 (1), 57—96. http://dx.doi.org/10.1016/S0889-9746(02)00099-3.

Pikovsky, A., Rosenblum, M., Kurths, J., 2001. Synchronization: A Universal Concept in Nonlinear Sciences. Cambridge University Press.

Poncet, P., 2002. Vanishing of mode B in the wake behind a rotationally oscillating circular cylinder. Phys. Fluids 14 (6), 2021–2023. http://dx.doi.org/10.1063/1.1479344.

Prasanth, T., Mittal, S., 2008. Vortex-induced vibrations of a circular cylinder at low Reynolds numbers. J. Fluid Mech. 594, 463–491. http://dx.doi.org/10.1017/S0022112007009202.

Prasanth, T., Premchandran, V., Mittal, S., 2011. Hysteresis in vortex-induced vibrations: critical blockage and effect of m^*. J. Fluid Mech. 671, 207–225. http://dx.doi.org/10.1017/S0022112010005537.

Sarpkaya, T., 2004. A critical review of the intrinsic nature of the vortex-induced vibrations. J. Fluids Struct. 19 (4), 389–447. http://dx.doi.org/10.1016/j.jfluidstructs.2004.02.005.

Schulz, K., Kallinderis, Y., 1998. Unsteady flow structure interaction for incompressible flows using deformable hybrid grids. J. Comput. Phys. 143, 569–597. http://dx.doi.org/10.1006/jcph.1998.5969.

Shen, L., Chan, E.-S., Lin, P., 2009. Calculation of hydrodynamic forces acting on a submerged moving object using immersed boundary method. Comput. & Fluids 38 (3), 691–702. http://dx.doi.org/10.1016/j.compfluid.2008.07.002.

Shiels, D., Leonard, A., Roshko, A., 2001. Flow-induced vibration of a circular cylinder at limiting stuctural parameters. J. Fluids Struct. 15 (1), 3–21. http://dx.doi.org/10.1006/jfls.2000.0330.

Singh, S., Mittal, S., 2005. Vortex-induced oscillations at low Reynolds numbers: hysteresis and vortex-shedding modes. J. Fluids Struct. 20 (8), 1085–1104. http://dx.doi.org/10.1016/j.jfluidstructs.2005.05.011.

Soti, A., Zhao, J., Thompson, M., Sheridan, J., Bhardwaj, R., 2018. Damping effects on vortex-induced vibration of a circular cylinder and implications for power extraction. J. Fluids Struct. 81, 289–308. http://dx.doi.org/10.1016/j.jfluidstructs.2018.04.013.

Tang, G., Lu, L., Zhao, M., Liu, M., Zong, Z., 2017. Phase jump and energy transfer of forced oscillating circular cylinder in uniform flow. Proc. Inst. Mech. Eng. M 231 (2), 496–510. http://dx.doi.org/10.1177/1475090216656950.

Vandiver, J.K., 2012. Damping parameters for flow-induced vibration. J. Fluids Struct. 35, 105–119. http://dx.doi.org/10.1016/j.jfluidstructs.2012.07.002.

Wang, E., Xiao, Q., Incecik, A., 2017. Three-dimensional numerical simulation of two-degree-of-freedom VIV of a circular cylinder with varying natural frequency ratios at $Re = 500$. J. Fluids Struct. 73, 162–182. http://dx.doi.org/10.1016/j.jfluidstructs.2017.06.001.

Wei, R., Sekine, A., Shimura, M., 1995. Numerical analysis of 2D vortex-induced oscillations of a circular cylinder. Internat. J. Numer. Methods Fluids 21, 993–1005. http://dx.doi.org/10.1002/fld.1650211016.

Williamson, C., Govardhan, R., 2004. Vortex-induced vibration. Annu. Rev. Fluid Mech. 36, 413–455. http://dx.doi.org/10.1146/annurev.fluid.36.050802.122128.

Williamson, C., Roshko, A., 1988. Vortex formation in the wake of an oscillating cylinder. J. Fluids Struct. 2 (4), 355–381. http://dx.doi.org/10.1016/S0889-9746(88)90058-8.

Yang, J., Preidikman, S., Balaras, E., 2008. A strongly coupled, embedded-boundary method for fluid–structure interactions of elastically mounted rigid bodies. J. Fluids Struct. 24, 167–182. http://dx.doi.org/10.1016/j.jfluidstructs.2007.08.002.

Zhang, W., Li, X., Jiang, Y., 2015. Mechanism of frequency lock-in in vortex-induced vibrations at low Reynolds numbers. J. Fluid Mech. 783, 72–102. http://dx.doi.org/10.1017/jfm.2015.548.

Zhao, M., Cheng, L., Lu, L., 2015. Vortex induced vibrations of a rotating circular cylinder at low Reynolds number. Phys. Fluids 26, 073602. http://dx.doi.org/10.1063/1.4886196, (28 pages).

Zhou, C., So, C., Lam, K., 2004. Vortex-induced vibrations of an elastic circular cylinder. J. Fluids Struct. 13 (2), 165–189. http://dx.doi.org/10.1006/jfls.1998.0195.